A Simulation of an Experiment to Measure the Initial State Helicity Correlation in Wide Angle Compton Scattering

Justin Lane Wright

Chesapeake, VA

B.S., Physics, The University of Virginia, 2003

A Thesis Presented to the Graduate Faculty
of the University of Virginia in Candidacy for
the Degree of Master of Science

Department of Physics
University of Virginia

January, 2007

Abstract

Many powerful tools have been developed in an attempt to describe nuclear interactions at various energy levels. It is clear that perturbative Quantum ChromoDynamics (pQCD) dominates at sufficiently high energy, whereas the "Handbag" model involving a single interacting quark dominates at sufficiently low energy. It is not clear which model is appropriate at energies of 1-10 GeV. The Initial State Helicity Correlation in Wide Angle Compton Scattering (WACS) experiment will shed light on this subject by measuring the polarization observable A_{LL} at $-t = 6.4$ GeV ($\theta_{CM} = 140\,\mathrm{deg}$) and at $-t = 2.4$ GeV ($\theta_{CM} = 70\,\mathrm{deg}$). In advance of this experiment a Monte-Carlo simulation using the Geant4 toolkit was used to examine various aspects of the experiment design. It was shown that the goals of this experiment, as laid out in its proposal, can be met using the available equipment and in the proposed amount of time. There is also evidence that the Monte-Carlo will prove useful as an analysis tool after the experiment has run.

Contents

Chapter 1

Introduction

In recent years, much work has been done to explore the nature of the nucleon in the realm of intermediate energies and momentum transfers. The construction of moderate energy electron beams at the Thomas Jefferson National Accelerator Facility (JLab) and other sites has allowed this exploration to take place. Some of the recent experiments have shown the usefulness of studying exclusive reactions at large momentum transfer.

Perturbative Quantum Chromodynamics (pQCD) was originally developed in the 1960's in hopes that nuclear interactions could be explained in much the same way as electro-magnetic interactions. Initially, pQCD found success at high energies, allowing the proper calculation of various cross sections and including the onset of scaling in Deep Inelastic Scattering (DIS) [1]. This success led many to believe that pQCD would also be useful at more moderate energies of around 5-10 GeV. Alas, this was not the case. pQCD has routinely underestimated cross sections in this regime, sometimes by an order of magnitude [2]. Several other experimental results have also disagreed with the predictions of pQCD. Measurements of the electric form factor of the proton G_E^p [3, 4] taken in 1998 indicated that nucleon helicity is not conserved, in direct

contrast to the precepts of pQCD. A measurement of the polarization observable K_{LL} in a Real Compton Scattering (RCS) experiment also strongly disagreed with the predictions of pQCD [5].

There is, however, an alternative theoretical framework that shows promise. The so-called "Handbag" model [6, 7, 8] seeks to explain hard, exclusive events as an interaction with a single, nearly free quark. But, of course, this model brings up just as many questions as it answers. If the Handbag model is to work, we must also be able to describe the nature of this nearly-free quark and how it couples to the rest of the nucleon system.

The Initial State Helicity Correlation in Wide Angle Compton Scattering (WACS) experiment, E05-101 [9], will seek to answer these questions and more. The proposal is to measure the polarization observable, A_{LL}, and compare the result to the predictions of both pQCD and the Handbag model. These data will complement the data already collected by experiments such as the RCS mentioned above.

The next chapter will discuss the motivations for carrying out this experiment in greater detail. Chapter 3 will cover the preparations necessary for WACS to run and the experimental setup. Chapter 4 will detail the workings of the Geant4-based Monte-Carlo simulation which was designed specifically for WACS, but may also prove applicable to any similar experiment in the future. The last chapter will present the results of these simulations and estimate the backgrounds we can expect from photo-nucleon and lepton-nucleon processes. Important pieces of source code for the simulation can be found in the appendices, along with a brief explanation of how to run the simulation.

Chapter 2

History and Motivations

2.1 Nature of Nucleons

The field of Nuclear Physics was born with the discovery of the finite size of the nucleon. The fact that nucleons contain structure was realized in the first half of the last century with the discovery of their irregular magnetic moments. Since then, the struggle has been to describe this structure and its implications. A major step was taken in 1968 when the first direct evidence of quarks was revealed. Since then the standard model of particle physics, which describes the world in terms of three basic types of particles; quarks, leptons, and force carriers, has been developed. There are a total of six quarks in three families, six leptons in three families and at least 12 force carriers. Each of the quarks and leptons also has an anti-particle counterpart with opposite charge. Information about the six quarks is given in Table 2.1. Due to their extremely large masses, the four most massive quarks do not play a role in ordinary matter.

In a loose sense, the relationship between nucleons and quarks is similar to the relationship between atoms and nucleons. For example, we know that a helium atom

Table 2.1: *The 3 families of quarks.*

Flavor	Charge (e)	Mass (GeV/c^2)
up	+2/3	0.004
down	−1/3	0.008
strange	−1/3	0.15
charm	+2/3	1.5
bottom	−1/3	4.7
top	+2/3	176

is made up of two neutrons and two protons, just as a proton is made up of two up quarks and one down quark. Things become more difficult, though, when we realize that nucleon structure does not start and end with the three valence quarks. Indeed, there also exists a sea of quark/anti-quark pairs in addiation to the valence quarks. Theoretically, this sea is composed of every type of quark and anti-quark, which can contribute, for example, a small amount of "strangeness" to otherwise ordinary matter.

The composition of a nucleon is not enough information to predict how it will behave, though. One must know how each component is distributed in order to make accurate calculations. The current paradigm is to describe the ground state properties of nucleons with various form factors. For example, at moderate energies (1-10 GeV) the elastic electric and magnetic form factors can be used to describe elastic electron scattering from a nucleon. In the non-relativistic limit, the electric form factor is the Fourier transform of the charge distribution of a particle in space. It can be written as

$$G_E(q^2) = F_1(q^2) - \tau F_2(q^2), \tag{2.1}$$

where F_1 and F_2 are the Dirac and Pauli form factors and q^2 is the square of the

4-momentum transfer. Here $\tau \equiv -q^2/4M^2$. The magnetic form factor, on the other hand can be seen as the Fourier transform of a current distribution and can be written as

$$G_M(q^2) = F_1(q^2) + F_2(q^2). \tag{2.2}$$

All of the information about the structure of a nucleon can be summed up in these two functions and they modify the cross section of a point particle in a very simple way:

$$\left(\frac{d\sigma}{d\Omega}\right)_{ns} \Rightarrow \left(\frac{d\sigma}{d\Omega}\right)_{ns} |F(q^2)|^2, \tag{2.3}$$

where the subscript "ns" indicates that the differential cross section on the left is for a particle with no structure. This fact makes elastic lepton scattering a very attractive probe of the nucleon, at accessible energies, as the leptons have no structure of their own.

When it comes to describing an interaction between two or more particles the structure of these particles is only half the story. The other key piece of information needed is a reaction mechanism. One must describe, in detail, how these particles couple to one another and one must account for every possible permutation of this coupling. Perturbative Quantum-Chromo Dynamics (pQCD) has developed into a very successful theory of nuclear interactions in the high energy arena. In Deep Inelastic scattering (DIS) as energies above 10 GeV, pQCD has correctly predicted many scattering cross sections, including the onset of scaling in Mandelstam-s at constant scattering angle. The subsequent observation of scaling in exclusive reactions at intermediate energies (1-10 GeV) leads to the assumption that pQCD may be applicable here as well [1]. Certain discrepancies between pQCD predictions and experimental observations [2] has lead to the positing of an alternative view, described

by the Handbag diagram. Recent evidence from an experiment at Jefferson Labs (JLab) [5] supports this model over pQCD. Each of these models, their merits and predictions will be discussed in the following Sections.

At this point it is necessary to define the variables that will be used to describe particle interactions throughout the rest of this thesis. It is most convenient to express a given interaction in the most general terms possible. For an interaction involving two initial particles and two final particles we define the kinematics as follows;

$$q_\mu + p_\mu \rightarrow q'_\mu + p'_\mu, \tag{2.4}$$

where $q(q')$ represents the incident (scattered) particle and $p(p')$ represents the target (recoil) particle. Lorentz invariant variables can be used to describe these interactions. The square of the momentum transfer is

$$Q^2 = (q-p)^2_\mu = 4E_q E_{q'} \sin^2\left(\frac{\theta_{qq'}}{2}\right), \tag{2.5}$$

where $\theta_{qq'}$ is the angle between $|\vec{q}|$ and $|\vec{q'}|$ and E is the total energy of the specified particle. The invariant Mandelstam variables are also used;

$$s = (q+p)^2_\mu = m_q^2 + m_p^2 + 2E_q E_p - 2\vec{q}\cdot\vec{p}, \tag{2.6}$$

$$t = -(Q^2) = (q-q')^2_\mu = m_q^2 + m_{q'}^2 - 2E_q E_{q'} + 2\vec{q}\cdot\vec{q'}, \tag{2.7}$$

$$u = (q-p')^2_\mu = m_q^2 + m_{p'}^2 - 2E_q E_{p'} + 2\vec{q}\cdot\vec{p'}, \tag{2.8}$$

where m is the mass of the specified particle. s is the total energy of the interaction, t is the momentum transferred from the incident particle to the scattered particle and u is the momentum transferred from the incident particle to the recoil particle. Together

these quantities can be used to describe the entire interaction in any reference frame

2.2 pQCD

Considering the success Quantum Electrodynamics has had in describing the electromagnetic force, it only makes sense to tackle the strong nuclear force with a similar theory. pQCD is the result of this attempt. Early problems arose when it became clear that the coupling constant in strong reactions is much larger than that of electromagnetic reactions. In short, a perturbative series does not necessarily converge in pQCD. This realization left the future of pQCD in question until it was realized that the coupling constant for the strong force is not a constant at all. Instead, it decreases as the momentum transfer increases so that quarks are essentially free at arbitrarily high energies (hence the phrase asymptotic freedom.) As a result, pQCD as been quite successful at high energies, where the coupling "constant" is small enough to allow convergence if the equations are handled properly. Here, "high energy" means that the momentum transfer should be much larger than the parton (quark) masses and transverse momenta. Here, transverse momentum refers to the component of the particle's momentum that is perpendicular to the beam axis in a particle experiment. This requirement has the side effect of strongly suppressing any non-valence quark contributions to a calculation [10], because the sea quarks cannot carry a great quantity of longitudinal momentum. Within these limitations, pQCD makes two predictions about exclusive reactions that are particularly worthy of note; hadron helicity conservation (HHC) [11] and constituent counting rules (CCR) [12]. These two predictions are of great importance because they can be easily tested experimentally by measuring polarization observables and differential cross sections, respectively. At energies above 50 GeV the predictions of pQCD have been quite successful [13]. The

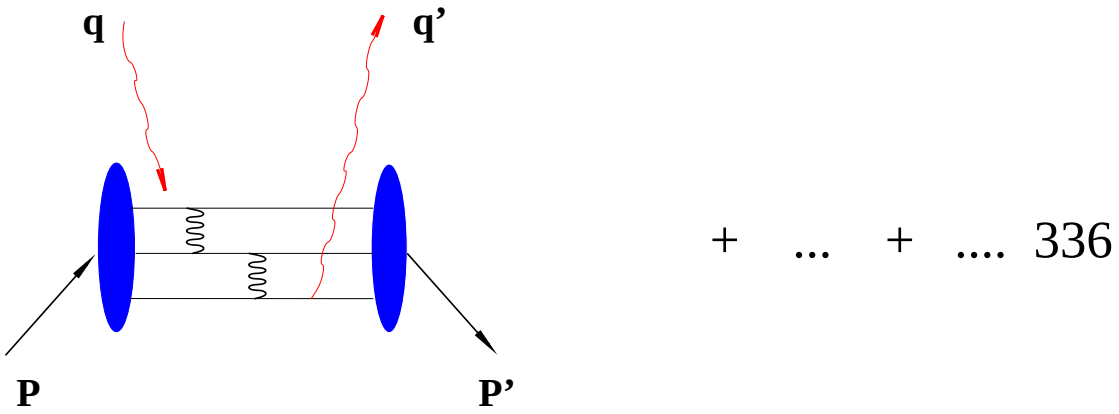

Figure 2.1: *Proton-Compton scattering in the pQCD model. The unprimed variables describe ingoing particles, while the primed variables describe outgoing particles. p and q are the 4-momenta of the proton and the photon respectively. The three quarks interact via two hard gluons. There are 336 permutations. [9]*

question is to what lower energy this success will extend. This experiment and a few other recent ones seek to answer this question by measuring at 1-10 GeV in the simplest of all exclusive reactions, Compton scattering.

Within the pQCD framework, proton-Compton scattering is represented by 336 permutations of Figure 2.1 [2, 14]. Essentially, the photon interacts with all three of the proton's valence quarks via the exchange of two hard gluons. These gluons distribute the momentum transfer throughout the nucleon and contribute to the hard scattering amplitude. This leads directly to the constituent counting rules mentioned above. Due to asymptotic freedom, these bound partons behave approximately as free particles when probed with a large momentum transfer. The differential cross section under these conditions can then be written

$$\frac{d\sigma}{dt} = \frac{f\left(\theta_{cm}\right)}{s^{n-2}}, \tag{2.9}$$

where s and t are the Mandelstam variables, f is some function of the scattering angle and n is the number of active constituents in the interaction. For fixed scattering

angle, the cross section of proton-Compton scattering is expected to vary linearly in s^{-6}, because there are three quarks and one lepton in both the initial and final states.

The Compton process can be factorized in the normal way into a hard part and two soft parts [13]. The photon scattering and gluon exchange described above is described by a hard scattering amplitude T. The two soft parts of the interaction are the initial and final states of the proton and these are described by valence quark distribution amplitudes $\phi_i(\vec{x})$ and $\phi_i(\vec{y})$, where $\vec{x}$ and $\vec{y}$ represent the quark momentum fractions and i labels the three-valence-quark Fock state of the proton. Using both the hard scattering amplitude and the two soft matrix elements, the helicity amplitudes for proton-Compton scattering [2, 15] can be written

$$\mathcal{M}^{\lambda\lambda'}_{hh'} = \sum_{d,i} \int_0^1 d\vec{x} d\vec{y} \delta \left(1 - \sum_{j=1}^{3} x_j\right) \delta \left(1 - \sum_{k=1}^{3} y_k\right) \times \phi_i(\vec{x}) T_i^d(\vec{x}, h, \lambda; \vec{y}, h', \lambda') \phi_i^*(\vec{y}), \tag{2.10}$$

where λ and λ' are the initial and final photon helicities, h and h' are the initial and final proton helicities and d indicates a sum over all contributing Feynman diagrams. The prediction of hadron helicity conservation arises from the hard part of this amplitude. All three constituent quarks participate and the helicity of each quark is conserved. This means that the overall helicity of the hadron must be conserved, ie. $\mathcal{M}^{\lambda\lambda'}_{\uparrow\downarrow} = 0$.

These helicity amplitudes contribute not only to spin-averaged cross sections, but also to polarization observables. If L, N and T represent the longitudinal (direction of particle motion), normal (out of interaction plane) and transverse (in plane) spin directions the coefficients for polarization transfers [7] can be written as:

$$K_{LL} \frac{d\sigma}{dt} = \frac{d\sigma(\uparrow\uparrow)}{dt} - \frac{d\sigma(\downarrow\uparrow)}{dt}, \tag{2.11}$$

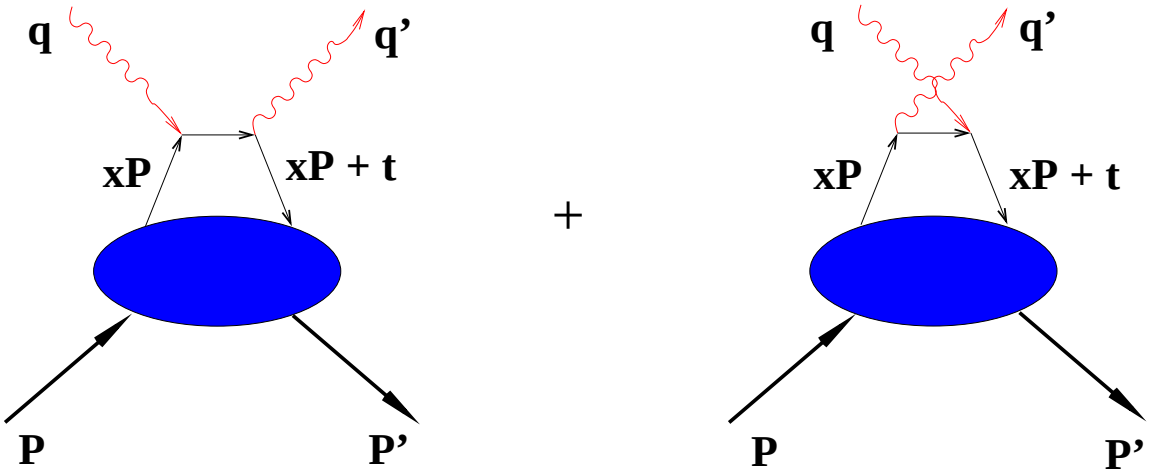

Figure 2.2: *Proton-Compton scattering in the "Handbag" model. The photon scatters from a nearly free quark and the momentum transfer is then distributed throughout the rest of the proton by numerous soft gluon exchanges. [9]*

$$K_{LT}\frac{d\sigma}{dt} = \frac{d\sigma(\uparrow\rightarrow)}{dt} - \frac{d\sigma(\downarrow\rightarrow)}{dt}, \tag{2.12}$$

and

$$K_{LN} = 0. \tag{2.13}$$

Here the first arrow represents the initial photon polarization and the second represents the recoil proton polarization. Hadron helicity conservation then requires that $K_{LL} = A_{LL}$, the helicity correlation between the two initial state particles. HHC also leads to the prediction that $K_{LT} = A_{LT} = 0$.

2.3 "Handbag" Models

The so-called "Handbag" model takes an entirely different approach to the real Compton interaction (RCS). It was first considered not long after the first direct evidence of quarks was published and has since been revived for other exclusive processes in addition to RCS. The two leading order diagrams are shown in Figure 2.2 [6, 16].

The primary difference between this formalism and pQCD is that the hard part of the interaction involves the photon scattering from a single structureless, spin-$^1/_2$ particle, which is easily calculable using pQCD and QED. The soft factor takes the form of generalized parton distributions (GPDs) [17, 18, 19, 20], which describe how the active quark couples to the rest of the nucleon. The four GPDs represent "super structures" of the proton and the other, more familiar, structure functions can be derived from them. As a result, the GPDs could be very useful in relating exclusive reactions to inclusive ones.

Only three GPDs come into play when describing RCS; $H(x,\xi,t)$, $\hat{H}(x,\xi,t)$, and $E(x,\xi,t)$. For each form factor, the skewness parameter, ξ, vanishes because both the initial and final state photons are real. As mentioned above, it is possible to write any proton form factor in terms of these GPDs, including the vector, axial and tensor RCS observables. They are, in order,

$$R_V(t) = \sum_i e_i^2 \int_{-1}^{1} \frac{dx}{x} H^i(x,0,t), \tag{2.14}$$

$$R_A(t) = \sum_i e_i^2 \int_{-1}^{1} \frac{dx}{x}\frac{x}{|x|} \hat{H}^i(x,0,t), \tag{2.15}$$

$$R_T(t) = \sum_i e_i^2 \int_{-1}^{1} \frac{dx}{x} E^i(x,0,t), \tag{2.16}$$

where e_i is the charge of the i^{th} active quark. These form factors can, in turn, be used to write the RCS helicity amplitudes within the "Handbag" model. Using the same convention for $\mathcal{M}_{hh'}^{\lambda\lambda'}$ as in the previous Section,

$$\mathcal{M}_{\uparrow\uparrow}^{\lambda\lambda'}(s,t) = 2\pi\alpha_{em}\left[\mathcal{H}_{\uparrow\uparrow}^{\lambda\lambda'}(s,t)(R_V(t)+R_A(t)) + \mathcal{H}_{\downarrow\downarrow}^{\lambda\lambda'}(s,t)(R_V(t)-R_A(t))\right], \tag{2.17}$$

$$\mathcal{M}^{\lambda\lambda'}_{\uparrow\downarrow}(s,t) = \pi\alpha_{em}\frac{\sqrt{-t}}{m}\left[\mathcal{H}^{\lambda\lambda'}_{\uparrow\uparrow}(s,t) + \mathcal{H}^{\lambda\lambda'}_{\downarrow\downarrow}(s,t)\right] R_T(t), \tag{2.18}$$

where $\mathcal{H}^{\lambda\lambda'}_{nn'}$ describes the hard scattering process and $n(n')$ is the helicity of the initial (final) state scattering quark. The vector, axial and tensor form factors mentioned above handle the soft part of the reaction.

These quantities are only useful to the experimentalist if they can be used to calculate actual cross sections and polarization observables. As mentioned above, the hard part of the process can be treated simply as elastic scattering from a structureless spin-$^1/_2$ quark. As a result, the spin-averaged cross section can be factorized [6, 16] and written as

$$\frac{d\sigma}{dt} = \frac{d\sigma_{KN}}{dt} f_V \left[R_V^2(t) + \frac{-t}{4m^2}R_T^2(t)\right] + (1-f_V)R_A^2(t), \tag{2.19}$$

where the suffix "KN" indicates the Klein-Nishina cross section and f_V is a kinematic factor. It is interesting to note that f_V is very near unity for large transverse momenta. In this case, the axial form factor is strongly suppressed in equation 2.19. With the spin-averaged cross section and the observables K_{LL} and K_{LT} it is then possible to determine all three of the RCS form factors, which in turn brings us close to determining all four of the GPDs. If the last GPD ($\hat{E}(x,\xi,t)$) is determined from a different type of experiment we will have a complete picture of the nucleon in the exclusive regime. The similarity between this reaction and other elastic reactions means that the information gathered here will be useful in all studies of the proton, not just those involving real photons.

Several predictions have been made for real Compton scattering using the "Hand-bag" model as described above. First of all, these models predict something close to the scaling behavior that arises from the constituent counting rules of pQCD. This

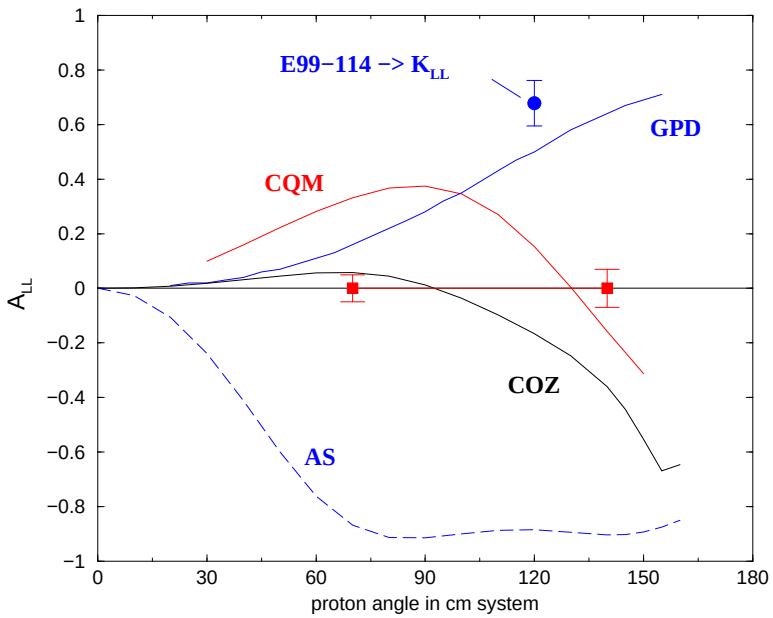

Figure 2.3: *Predictions for ALL and K_{LL} using the GPD [7] and CQM [21] approaches, along with the single measurement of K_{LL} made by the previous RCS experiment and the two measurements that will be made by WACS. COZ and AS are two predictions made by pQCD models.*

comes about due to the broad maximum in the RCS form factors, R_V, R_A and R_T around $-t = 8$ GeV^2. There are also predictions for the polarization observables A_{LL} and K_{LL}. Kroll et. al. [7] used the GPD formalism with massive quarks, but ignored hadron helicity flip. These calculations led to the prediction that $A_{LL} = K_{LL}$, just as in pQCD. G.A. Miller [21], on the other hand, used a constituent quark model with massless quarks and included hadron helicity flip. This led to the prediction that A_{LL} and K_{LL} diverge as the scattering angle increases and that A_{LT} and K_{LT} are non-zero. Miller found that these differences come down to a factor of the ratio of the tensor form factor to the vector form factor. That is to say,

$$K_{LL} = A_{LL} + \mathcal{O}(\kappa_T), \tag{2.20}$$

and

$$K_{LT} = -A_{LT} + \mathcal{O}(\kappa_T), \tag{2.21}$$

where

$$\kappa_T = \frac{\sqrt{-t}}{2m}\frac{R_T}{R_V}. \tag{2.22}$$

Since the form factors used in elastic photo-nucleon scattering are linked to the form factors used in RCS via GPDs it is possible to estimate the value of κ_T based on the measured ratio of the Pauli and Dirac form factors. This gives $\kappa_T \simeq 0.37$ for large $-t$. This is very different from the other models' predictions of $A_{LL} = K_{LL}$ and will be one of the easiest ways to distinguish between the two "Handbag" models presented here. The predictions of Kroll et. al. [7] and Miller [21] for A_{LL} have been plotted in Figure 2.3, along with the predictions of two pQCD models.

2.4 Past Results and WACS Physics Goals

So far two major experiments have been performed to test real Compton scattering at backward angles and energies of order one GeV. The first was an experiment at Cornell [22] that measured the cross section at seven kinematics points. This experiment immediately challenged the idea that pQCD might be applicable here by recording cross sections that were nearly an order of magnitude larger than pQCD predicts. On the other hand, these measured cross sections are within a factor of two of the calculations made using the "Handbag" model. These data were, however, consistent with the pQCD prediction of scaling in s^{-6}.

A second experiment was recently performed in Hall A at JLab [23] that attempted to measure both the longitudinal and transverse polarization transfer observables (K_{LL} and K_{LT}). The results of this experiment also called the pQCD approach into

doubt. K_{LL} was measured to be large and positive while K_{LT} was measured to be small and positive. As mentioned in Section 2.2, pQCD requires that $K_{LT} = 0$ and predicts that K_{LL} is small and negative. Indeed, the value measured for K_{LL} was nearly as high as the value predicted for hard scattering from a free quark. This is completely inconsistent with the pQCD picture of three active quarks. It should be noted, though, that the measurement of K_{LT} was nearly consistent with zero and these observables were only measured at a single kinematics point. Clearly more data is needed before pQCD is abandoned in this regime.

The Initial State Helicity Correlation in Wide Angle Compton Scattering (WACS) [9] experiment will attempt to compliment the small existing data set by measuring the polarization observable A_{LL} at two kinematics points, one at a greater scattering angle ($\theta_{CM} = 140^o$) than the Hall A measurement and the other at a smaller angle ($\theta_{CM} = 70^o$). These measurements will provide four key pieces of information, which will help to distinguish between pQCD and the "Handbag" model as the dominant model at these energies. They are:

1. The RCS cross section.

2. The magnitude and sign of A_{LL}.

3. The difference (if any) between A_{LL} and K_{LL}.

4. The difference (if any) between A_{LT} and zero.

This additional data will then either support or refute the pQCD predictions of hadron helicity conservation and constituent counting rules. In so doing, it will also either support or refute the predictions made by the "Handbag" model and perhaps distinguish between the models of Miller and Kroll et.al.

Chapter 3

Experimental Design

The Initial State Helicity Correlation in Wide Angle Compton Scattering experiment (WACS) will attempt to measure the polarization observable A_{LL} at two kinematics points, in the reaction $\gamma + p \rightarrow \gamma + p$ [9]. This measurement will require a beam of 4.3 GeV photons and a polarized proton target. The scattered photons will be captured by a calorimeter and the recoil protons will be detected by the high momentum spectrometer (HMS), a standard piece of equipment in Hall C. The setup for this experiment is shown schematically in Figure 3.1, with the exception that the HMS and calorimeter arms should switch sides. The coordinate convention used here is to consider the $+z$ axis to be the direction of the primary electron beam. The $+y$ axis is defined to be in the vertical direction and this means the $+x$ axis points to the left for a viewer looking in the beam direction. It is then most convenient to place the origin at the center of the target cell. This means that the HMS is on the $-x$ side of the beam and the calorimeter is on the $+x$ side of the beam. The local coordinates of the detector planes will be defined in the final chapter.

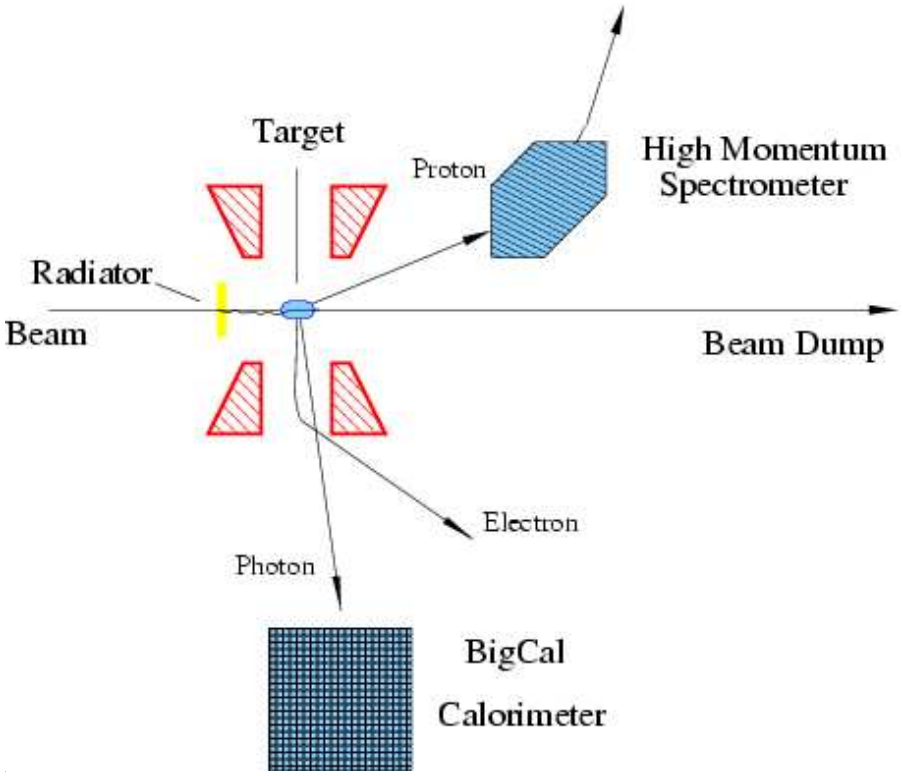

Figure 3.1: *The experimental setup for WACS. Not to scale.*

3.1 Beam and Radiator

The Thomas Jefferson National Accelerator Facility (JLab) in Newport News is one of the few laboratories in the world capable of carrying out an experiment like WACS. Its "racetrack" style accelerator is easily capable of delivering the desired 90 nA of 4.8 GeV electrons with a polarization of up to 80% and a duty factor of 100%. The polarization of the beam can be measured to within 3% by the Hall C Moeller polarimeter.

The photons for this experiment will be created via the hard bremsstrahlung process as the electron beam passes through a thin copper radiator. This process has the side effect of spreading out the beam (both electrons and photons) in the x and y directions. As a result, placing the radiator farther from the target cell causes more

stray particles to hit structures within the target outer vacuum can. In the past it was believed that this effect should be limited as much as possible by placing the radiator as close to the target cell as the geometry of the target can would allow. The downside to this design is that during the experiment the radiator will be much more difficult to handle if it is inside the target outer vacuum can. For WACS it was decided that the additional background is well worth the convenience of having easy access to the radiator. As a result, the radiator will be placed outside the target refrigerator can, about 60-70 cm upstream of the target center.

The radiator will have a thickness equal to 10% of a radiation length (1.43 mm,) where a radiation length is defined as the thickness a material would have to be to attenuate the energy of incident particles by a factor of 1/e. This will create photon and electron spectra as shown in Figure 3.2. The incident electron beam will have an energy of 4.8 GeV, which will result in a mixed photon and electron beam at the target. Both particles will have energies ranging up to the incident beam energy of 4.8 GeV. The experiment is designed to use photon energies centered at 4.3 GeV. This energy is chosen for two reasons. First, the ratio of post-bremsstrahlung electrons to photons increases rapidly as one approaches the incident electron energy. This will increase the difficulty of sifting through the elastically scattered electrons in search of the elastically scattered photons. Second, the error in the photon energy is proportional to the slope of the energy spectrum. As can be seen in Figure 3.2, the photon spectrum drops off quickly near the incident electron energy and this area must be avoided.

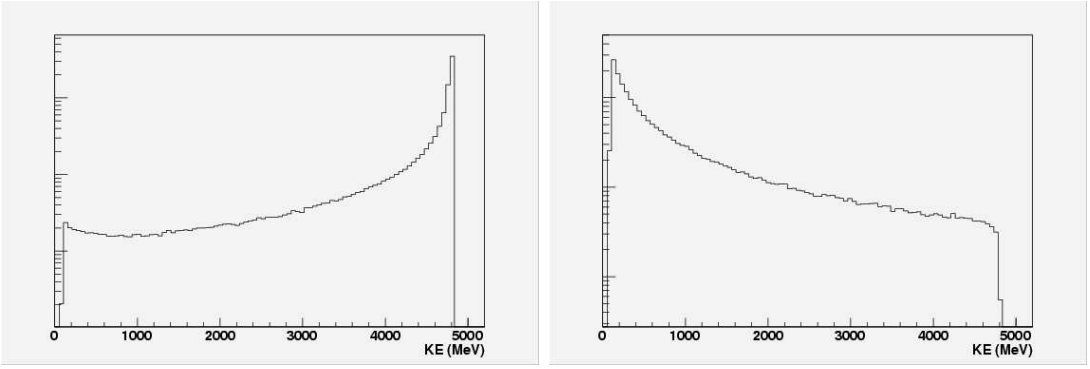

Figure 3.2: *The bremsstrahlung spectra of electrons (left) and photons (right) on a log scale from Geant4. A low energy cutoff of 100 MeV was applied to the simulation to prevent an asymptote at the origin.*

3.2 Polarized Ammonia Target

The polarized protons will be provided by the University of Virginia polarized target group [24, 25]. Figure 3.3 is a cross section of the target can. The target material will be solid $^{14}NH_3$. The target uses a technique known as dynamic nuclear polarization (DNP) to achieve proton polarization of up to 95% under ideal conditions. The target material is created by freezing gaseous ammonia into a white, crystaline solid. This solid ammonia is then irradiated with low energy electrons to create paramagnetic centers within the solid via electron knock-out. This process gives the ammonia a deep purple hue. During the experiment the material will incur radiation damage, which will reduce the maximum attainable polarization. Most of this damage can be repaired, though, by periodically annealing the material at 80 K. When the target is exposed to the beam, the level of polarization will decrease by a few percent due to the added heat load from the beam.

The target outer vacuum can (OVC) consists of an aluminum shell enclosing a thinner, 77 K shield. The shield is cooled by the liquid nitrogen reservoir and is used to protect the cooler parts of the system from inbound thermal radiation. The OVC

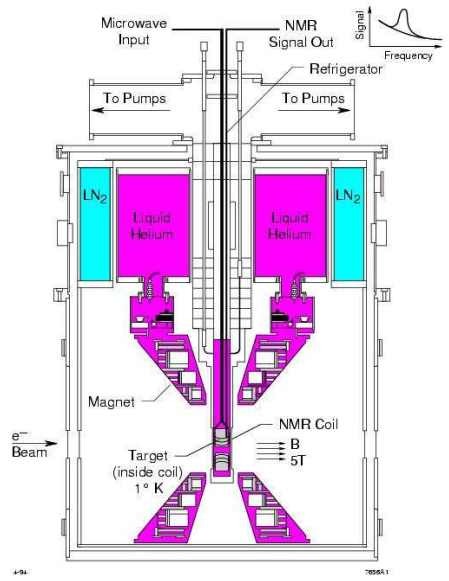

Figure 3.3: *Cross section of the UVa/Hall C solid polarized target.*

will have a thin beryllium window at the beam entrance and various thin aluminum windows for particle exits. The actual dimensions of these windows can be found in Section 4.3. The target magnet sits inside the shield, centered on the target cell, which is inserted into the refrigerator on the end of a long target stick. This stick also provides access to the target for the RF waveguide and the NMR circuit wiring. The entire cell is immersed in a bath of liquid helium which has been cooled to 1 K by a high power evaporation refrigerator.

The polarization process starts with the induction of a small natural polarization in the protons by placing the material in a strong magnetic field (5 T.) The natural polarization can be written,

$$P = \tanh \frac{\mu_p B}{kT}, \tag{3.1}$$

where μ_p is the magnetic moment of the proton, k is Boltzmann's constant, B is the magnitude of the magnetic field and T is the temperature. Under the circumstances listed above, proton polarizations are typically P $\sim$0.5%, but the electrons in the

material will reach a very high polarization (P ~100%) due to their much larger magnetic moment. Dynamic nuclear polarization (DNP) is used to transfer the spin of a polarized electron to an unpolarized proton. This process is facilitated by introducing an RF field near the electron resonance frequency. For a 5 T magnetic field the proper frequency is about 140 GHz. The DNP process can be more thoroughly understood through the theory of equal spin temperature [26], but that is beyond the scope of this paper.

Due to the nature of the energy level split in the electron-proton system, it is possible to change the direction of the proton polarization by simply changing the RF field. Going slightly above the electron resonant frequency will polarize the protons anti-parallel to the applied magnetic field, while going below the resonant frequency will result in a parallel proton polarization. Some of the systematic errors involving the target can be reduced by running for equal amounts of time with each polarization. For this reason, the polarization direction will be flipped after every anneal.

3.3 Detectors

In the WACS experiment the scattered photon will be captured by the same calorimeter that was built for G_E^p-III (see Figure 3.4 and Ref. [27].) It is composed of 1750 Pb-glass blocks of type TF-1 in 32 columns and 56 rows. All of which will be enclosed in a light-tight box. The recoil proton will be captured by a standard piece of Hall C equipment, the high momentum spectrometer (HMS.) The calorimeter will only be read out when the spectrometer detects a proton. This, combined with the energy threshold of the calorimeter (some hundreds of MeV,) will eliminate most of the electromagnetic background. Only elastic electron scattering events, proton-Compton events, and photons from π^0 photo-production, as well as a few rarer processes, will

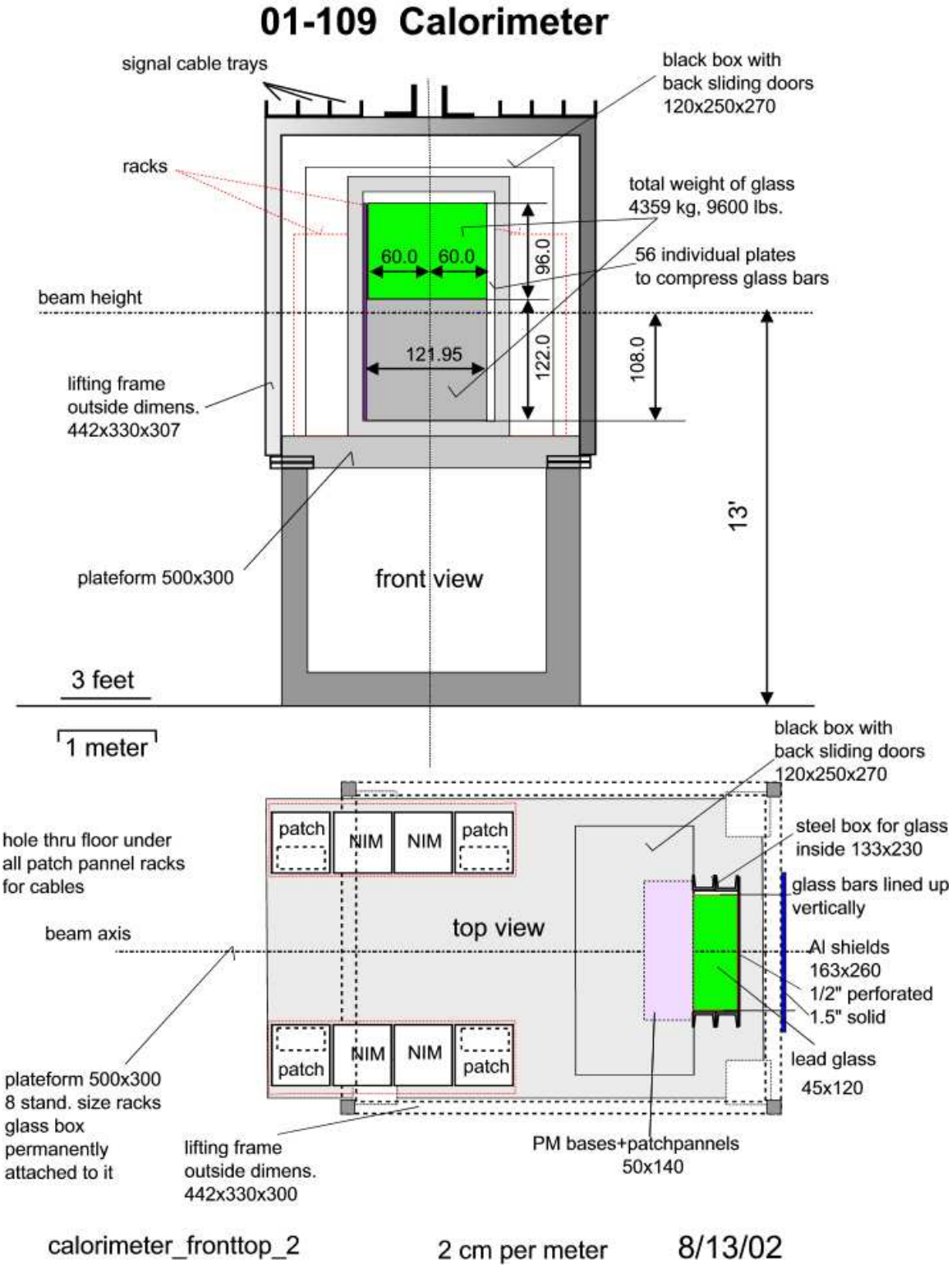

Figure 3.4: *The calorimeter, its electronics and its supporting structure [27].*

be recorded.

The calorimeter used in a previous RCS experiment had an energy resolution of 5.5% [9], and it is reasonable to expect a similar resolution on BigCal. Radiation damage of the scintillating bars nearly doubled this value by the end of that experiment, but the total beam charge collected by BigCal in this experiment (WACS) will be about two orders of magnitude less. For this reason, BigCal is expected to maintain a relatively constant energy resolution throughout the entire production phase. Should the effects of radiation damage become noticeable, it is possible to repair the blocks by irradiating them with ultraviolet light, but this process can take up to two weeks.

The HMS is a spectrometer consisting of three quadrupole magnets and a dipole. The quadrupoles serve to focus and transport the charged particles, while the dipole bends them vertically upward into the detector hut and disperses them onto the detector package. Here, the momentum of the particle can be determined by the amount of deflection caused by the dipole. The HMS has a resolution of $\Delta p/p < 0.1\%$ and its momentum acceptance is $\pm 8\%$ of the central momentum setting. It should also be noted that the distance between the calorimeter and the target was selected so that the solid angle subtended by BigCal would match the HMS acceptance.

3.4 Proposed Measurements

The two kinematic points of interest involve placing the calorimeter at an angles of $\theta_\gamma^{lab} = 25^\circ$ ($\theta^{CMS} = 70^\circ$) and $\theta_\gamma^{lab} = 82^\circ$ ($\theta^{CMS} = 140^\circ$) (see Table 3.1.) The angle for the HMS was calculated using the equations for elastic scattering. Both angles are for production data runs, but the forward angle will also be used to calibrate the calorimeter using elastically scattered electrons. The calorimeter will have to

be placed much farther from the target when at the forward angle ($L = 7.0$ m, as opposed to $L = 2.5$ m,) in order to keep the signal from being saturated by the higher event rates and to better match the acceptance of the HMS, as mentioned above.

Table 3.1: *The two kinematics points to be explored (all angles are in degrees.) The angles are given for the scattered particle (γ or e^-) and the recoil proton (p) in both the lab and center of momentum (CM) frames. The scattered particle energy (E_γ^{lab}) is given along with the recoil proton momentum (p_p^{lab}.) L is the distance from the target center to the center of the calorimeter, and the two deflection angles (θ_{def}) give the angular displacement of the electrons and protons at the detectors due to the target magnetic field.*

	$-t\,(\frac{\text{GeV}}{\text{c}})^2$	θ_γ^{lab}	θ_p^{lab}	E_γ^{lab} (GeV)	$p_p^{lab}\,(\frac{\text{GeV}}{\text{c}})$	L (m)	θ^{CM}	θ_{def}^e	θ_{def}^p
P1	2.4	25	39	3.00	2.02	7.0	70	1.7	4.1
P2	6.4	82	12	0.87	4.25	2.5	140	15.4	0.6

3.5 Signal and Backgrounds

In this exclusive experiment both the scattered photon and the recoil proton will be detected and their momenta measured. This provides us with a powerful means of limiting the background. The dipole magnet of the spectrometer can be set to ensure that only particles with positive charge will be detected. Furthermore, the narrow momentum acceptance of the HMS will ensure that almost every HMS event is the result of a recoil proton from a nearly elastic event. This means it is only necessary to read out the calorimeter every time a hit is detected in the HMS. With this discrimination in place only nuclear events will be recorded and the electromagnetic events (which have different kinematics) will be ignored. The electromagnetic background can be reduced further by setting the threshold on the calorimeter to some hundreds of MeV. In so doing, it will be guaranteed that only elastic and nearly-elastic events will survive the initial cut.

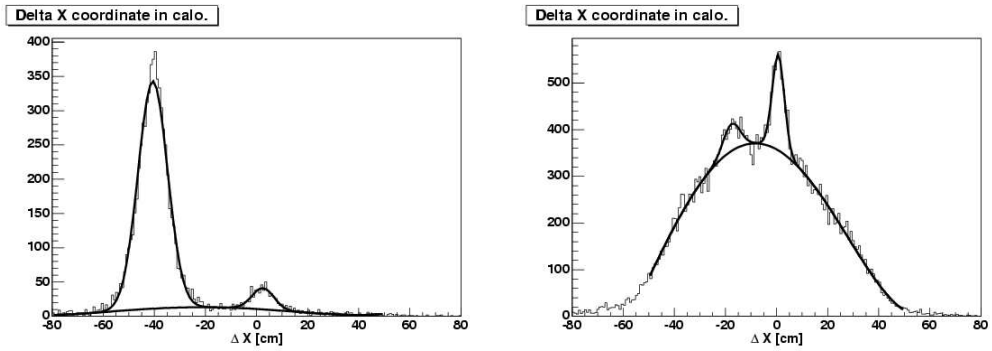

Figure 3.5: *Experimental data from the exclusive Compton scattering experiment [9]. They show the number of events versus the horizontal displacement of the event relative to its reconstructed detection location. The data on the left was taken at $E_\gamma = 4.3$ GeV and $\theta^{cm} = 73°$, while the data on the right was taken at the same energy and $\theta^{cm} = 128°$. The broad background is due to photons from the decay of neutral pions. The sharp peak near $\Delta x = 0$ in each image is from Compton photons, while the other sharp peak is from elastically scattered electrons.*

The background from non-electromagnetic processes will be much harder to reduce, however. There are two main sources of this non-electromagnetic background that could mimic a real Compton event. The first is elastic electron scattering from the proton. This event is kinematically identical to proton-Compton scattering because the mass of the electron is so small compared to the energies involved. The second main source of the non-electromagnetic background is neutral pion photoproduction from the proton. In this case, the mass of the pion is not negligible, but it is small enough that some of these events will interfere with the elastic scattering measurement.

As mentioned above, the elastic electron scattering has the same kinematics as real Compton scattering, but the cross section is quite different. The electron is a spin 1/2 particle that scatters via the exchange of a virtual photon. Evidence from Jefferson Lab experiment E99-114 (RCS) indicates that the ratio of the electron cross section to the Compton cross section decreases as the scattering angle increases (see Figure 3.5 and Ref. [9].) Add to this the fact that there are a great deal more electrons

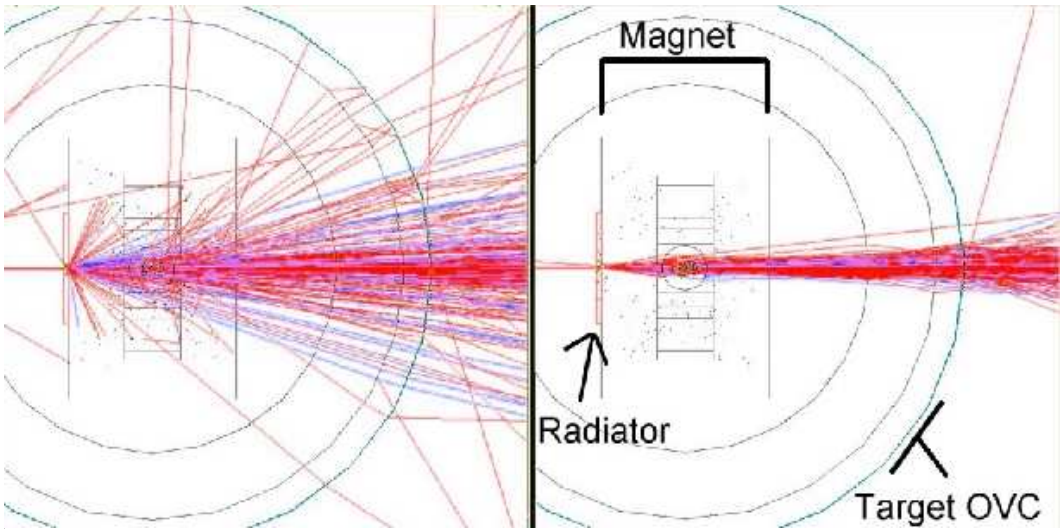

Figure 3.6: *Two wire-frame drawings of the target refrigerator can with target stick, magnet and particle tracks. The target magnetic field is off in the left image and on in the right image. In both cases, a low energy electron beam incident on a radiator near the target center created low energy charged particles. The target field is seen to trap these particles along the beamline.*

scattering from the target and the problem becomes evident, especially at the forward angle. The RCS experiment handled this problem by using a deflection magnet. The electrons were deflected by a small angle in the horizontal direction resulting in the electron and gamma peaks being Δx $\simeq$ 20 cm apart at the calorimeter. Figure 3.5 plots the number of events versus the horizontal correlation parameter. This parameter is defined as

$$\Delta x = x_{meas.} - x_{recon.}, \tag{3.2}$$

where $x_{meas.}$ is the actual position at which the event was detected and $x_{recon.}$ is the expected point of detection based on the proton kinematics measured in a spectrometer. The separation between the elastically scattered electrons and Compton photons is over 20 *cm*. It can also be seen that the elastically scattered electron peak becomes dominant relative to the Comtpon peak at forward angles, whereas the opposite is true at backward angles.

WACS will also deflect the scattered electrons, but will not require a new piece of equipment to do so. The field from the target magnet will be doing this job anyway. Near the target, this field is pointed in the direction of the beam and it will deflect both the electrons and the recoil protons vertically in the lab. The expected angles of deflection are given as θ^e_{def} and θ^p_{def} in Table 3.1. These angles were obtained from a ray tracing program, not the Geant4 simulation [28]. The results of the simulation will appear in Chapter 5. At both of the kinematics points, this deflection should result in Δy $\sim$ 10 cm, which is much greater than the spatial resolution of the calorimeter. An interesting side-note is that, while the target magnet deflects high energy charged particles vertically, it also tends to trap low energy charged particles along the beamline. This feature was recorded during early testing of the Geant4 simulation (see Figure 3.6.)

Chapter 4

Monte-Carlo Simulation

The goal of this simulation was to build into Geant4 the experimental apparatus described in the previous chapter along with the non-electromagnetic processes mentioned above and then simulate the data that will be taken during the WACS experiment. The specific questions that needed to be answered were as follows:

1. What is the total deflection of all particles due to the geometry of the target and the target field?

2. What is the Compton signal strength relative to the elastic and neutral pion backgrounds?

To this end, it was necessary to recreate each of the major pieces of equipment within Geant4, including the target can, the beam pipes, the HMS and the photon calorimeter. It was also necessary to develop ways to handle the different types of processes that can occur during a typical event. The electromagnetic processes have already been built into the standard Geant4 installation. The more complicated non-electromagnetic processes, on the other hand had to be added in by the author.

It was determined that the simulation should be broken up into three different parts. First, the primary electron beam should be simulated with only electromagnetic events turned on. With this setting, the mixed photon-electron beam could be studied at the target cell as well as the electromagnetic backgrounds in BigCal and the HMS. After that, the non-electromagnetic processes were simulated as primary events generated within the target. Each of these processes was handled separately and the events were generated with a flat distribution over the solid angle of interest. The last step was to re-normalize this data with the necessary cross sections and initial particle energy spectra.

4.1 Geant4

Geant4 is a free toolkit developed by physicists the world over and maintained on the CERN website [29]. It is designed to simulate the transport of particles through matter and capable of doing so on a wide energy scale (from a few keV to over 100 GeV.) A detector geometry of any complexity can be created in an experimental area of any size. Materials can be defined based on every physical property imaginable, including molecules, isotopes and ions. All common particle and many rare particles have also been included in Geant4's repertoire. Every electro-magnetic processes have been included in the standard release and are parameterized to cover almost the entire experimentally accessible energy range. Some hadronic interactions have been included as well, but the lepto-nuclear and photo-nuclear processes had not yet been developed at the time of this work. Each aspect of the simulation is tied together by a sophisticated management routine, giving the user complete control and flexibility.

The series of calculations made during a single run are designed to speed up the simulation process as much as possible without sacrificing too much accuracy. Many

of the calculations are done prior the tracking and this data is used to fill various tables which can be accessed by the event manager later. A typical simulation run starts by loading all of the necessary material, particle and physical process information into memory and then filling data tables with cross sections and mean free paths. These data tables will later be used to determine if and when a particular process will be used on a particle. Then the actual geometry of the user's system is built, including all physical objects and fields. Once this is done, the primary generator creates a single primary event consisting of one or more particles. These particles are then passed to the event manager as individual tracks. The event manager then uses the tracking manager to step each of these particles through the defined geometry. As interactions occur, new particles are created, tracked and destroyed based on the pre-loaded physics tables mentioned above. Naturally, the kinematical specifics of each interaction must be randomly sampled during the tracking process, but only after it has been established that this type of reaction will occur.

4.2 Materials and Particles

Geant4 provides the means to define virtually any substance one can conceive. Definitions for most of the elements and many common substances are already included in the Geant4 installation and the user is free to modify these or create their own definitions. The most common method defining a new element is to simply provide the atomic number, weight and density. Molecules can be created by providing the density and the number and type of each elemental component. Non-molecular materials can be created by providing the density and the mass fraction of each of the components. From this relatively small set of data the Geant4 toolkit calculates the density of nucleons and electrons in the material and uses this information to calcu-

late the probability of a particular electro-magnetic event occurring as an energetic particle passes through.

Most of the materials used in this simulations were given the standard definitions provided in the Geant4 release. Aluminum, Copper, and the other natural elements were defined in this way. Air was defined as 70 percent nitrogen and 30 percent oxygen by mass with a density of 1.290 mg/cm^3. Vacuum was defined simply as a proton gas at very low pressure. The simulated ammonia for the target was a combination of liquid helium and solid ammonia. It was 12 percent helium by mass and 88 percent ammonia, which corresponds to a packing fraction of about 0.5. In the actual experiment the packing fraction will be closer to 0.6, but 0.5 was used here. For liquid helium a density of 0.1249 g/cm^3 was used and for the solid ammonia, a density of 0.9 g/cm^3 was used. These values vary from the actual densities, which are 0.145 g/cm^3 and 0.867 g/cm^3, respectively.

In addition to the physical materials, it is also possible to define nearly any type of particle. The difference between the two being that, in Geant4, particles can carry momentum and do not have constituent parts. The Geant4 toolkit provides definitions for almost every particle common to the nuclear realm. Everything from neutrinos to heavy exotics have already been created. For the WACS experiment only a handful of these particles were necessary, including: γ, e^-, e^+, μ^-, μ^+, π^0 and p. While it is possible for a 4.8 GeV electron beam to create a great many more particles, only these listed types are significant. Each of the above particles has been defined with its characteristic mass, charge and quantum numbers. While it is possible to also define some more complex quantities, like particle helicity, such detail was not necessary for a background study. Here it should also be noted that there is a distinct difference between the gamma particle and the optical photon as defined by Geant4. For those interested in real Compton experiments, the gamma is the desired definition.

4.3 Included Processes

As mentioned above, all of the standard electro-magnetic interactions have been accounted for in the Geant4 installation. The user has freedom to include or exclude these processes as necessary and to define the order in which the processes will be implemented for each individual particle in the simulation. The processes are divided into continuous and discrete categories, representing the nature of the process. They can also be applied to a given particle only at a specific point during the particle's motion, such as when the particle is at rest, at the end of a tracking step or during a tracking step. There is one general process that is common to all particles. This is the transportation process, which Geant4 uses to propagate every particle between detector volumes and through fields. Every other process is specific to one or a group of particles.

There are four processes included for gamma particles. They include:

1. Conversion to an e^-/e^+ pair
2. Conversion to a $\mu/\bar{\mu}$ pair
3. Photoelectric effect
4. Compton scattering from a bound electron

These are all discrete processes and do not require an order of precedence. The parameterized cross section used for Compton scattering from bound electrons is the following:

$$\sigma(Z, E_\gamma) = P_1(Z)\frac{log(1+2X)}{X} + \frac{P_2(Z) + P_3(Z)X + P_4(Z)X^2}{1 + aX + bX^2 + cX^3}, \tag{4.1}$$

where Z is the atomic number of the medium, E_γ is the energy of the incident photon,

m is the electron mass, $X = E_\gamma/mc^2$ and $P_i(Z) = Z(d_i + e_i Z + f_i Z^2)$. The values of the parameters are designed to fit experimental data (from Ref. [30] and Ref. [31]) taken over a wide range of energy and Z. The accuracy of the fit is estimated to be $\Delta\sigma/\sigma \leq 6\%$ [32]. The final energy of the photon is then sampled according to the Klein-Nishina differential cross section per atom [33],

$$\frac{d\sigma}{d\epsilon} = \pi r_e^2 \frac{m_e c^2}{E_0} Z \left(\frac{1}{\epsilon} + \epsilon\right) \left(1 - \frac{\epsilon \sin^2\theta}{1+\epsilon^2}\right), \tag{4.2}$$

where r_e is the classical electron radius, m_e is the electron mass, E_0 is the incident photon energy, E_1 is the scattered photon energy and $\epsilon \equiv E_1/E_0$. The total cross section for the pair production (conversion) process is parameterized as

$$\sigma(Z, E_\gamma) = Z(Z+1)\left[F_1(X) + F_2(X)Z + \frac{F_3(X)}{Z}\right], \tag{4.3}$$

where $X = ln(E_\gamma/m_e c^2)$ and the functions F_n are fifth order polynomials in X. The coefficients of these polynomials have been used to fit the data from [30]. The final state is sampled from a form of the relativistic Bethe-Heitler formula that has been corrected for various effects [34]. The cross sections for conversion to a muon pair and the photoelectric process were both similarly parameterized and the final states sampled from an appropriate equation. Information about the conversion to muons process can be found in Ref. [32] and Ref. [35]. Lastly, the photoelectric effect has been parameterized and the final state electron's polar angle is sampled from the Sauter-Gavrila distribution [36]. Each of these methods are valid over a wide range of energy and atomic number, usually from around 10 keV to 100 GeV and from Z = 1 to 100. The accuracies are typically between 5 and 10%. More information can be found in the Geant4 Physics Reference Manual [32].

Three processes have been provided for the electron and the positron. They are, in order of precedence:

1. Multiple scattering
2. Ionization of an atom
3. Bremsstrahlung

Other processes such as synchrotron radiation have been excluded due to the small amount of energy change involved. Obviously, the bremsstrahlung process is the most important process to the WACS experiment because it is the source of the real photon beam. The total cross section per atom for bremsstrahlung was parameterized as

$$\sigma(Z, E_e, k_c) = Z(Z + \xi_\sigma)(1 - c_s Z^{1/4}) \left[\frac{E_e}{k_c}\right]^{\alpha} \left[\frac{\dot{f}_s}{N_{Avo}}\right], \tag{4.4}$$

where Z is the atomic number, E_e is the incident electron energy and f_s is a polynomial in $x = \ln E_e$ and k_c is a low-energy cut off. The rest of the symbols represent various constants. The energy loss sampling is handled by another parameterization in the same variables. It is also proportional to a polynomial in $x = \ln E_e$ [32]. Figure 3.2 shows the post-bremsstrahlung spectra created by 4.8 GeV electrons incident on a 1.43 mm copper radiator. These are the spectra of the photons and electrons that will be incident upon the target during the production phase of WACS.

The ionization process is treated as an energy loss process for the incident particle. Below a certain threshold (T_{cut},) the energy loss is considered to be continuous and no delta ray is produced. Above this threshold, the energy loss becomes discrete and is treated using the equations of Møller scattering (e^-e^-) or Bhabha scattering (e^+e^-) [32]. The energies involved in this simulation are much higher than $T_{cut} \sim 1keV$, so every ionization event will be a discrete event. The total cross section per atom for

Møller scattering [37] is

$$\sigma(Z, E, T_{cut}) = \frac{2\pi r_e^2 Z}{\beta^2(\gamma-1)}\left[\frac{(\gamma-1)^2}{\gamma^2}(\frac{1}{2}-x)+\frac{1}{x}-\frac{1}{1-x}-\frac{2\gamma-1}{\gamma^2}ln\left(\frac{1-x}{x}\right)\right], \tag{4.5}$$

where $\gamma = E/mc^2$, $\beta^2 = 1-(1/\gamma^2)$ and $x = T^{cut}/(E-mc^2)$. A similar equation gives the cross section for Bhabha scattering.

As a particle travels through matter it undergoes many small scattering events off the atoms that make up the material. This effect is handled by the multiple scattering process. It is based upon the work of Lewis [38] but is not an exact calculation of the particle's motion. In order to cut down on computations each individual scattering event cannot be calculated exactly. Instead, the Geant4 implementation uses a model designed to give the same results as the Lewis theory [32].

Positron annihilation has also been included, but only for at rest electrons and only for the case of two final state photons. Annihilation to anything other than two photons is considered to be negligible. The Heitler formula [34] is used to calculate the cross section for annihilation. In order to sample the final state, the energy limits of the gammas must first be determined. After that the energy can be randomly selected from this range, using the cross section mentioned above. The final angles are then defined by conservation requirements.

For the neutral pions only one process was actually necessary. Due to the extremely short lifetime of the particle, only decay need be considered. Furthermore, though the neutral pion has many different decay modes, only the decay into two photon case carries any significant weight. In the center of mass frame, these two photons travel in opposite directions with opposite momentum equal to half the rest mass of the neutral pion. The final momenta of these photons is sampled according to these kinematics, while the mean free path and physical interaction length are

calculated from the particle's mean lifetime. For pions with energy $E_\pi \sim 1GeV$ the mean free path is smaller than nuclear radii and thus, negligibly small in terms of electromagnetic interactions. This means the pions always decay before they have a chance to interact with other materials in the simulation. The fact that pions and recoil protons can interact with their parent nuclei is taken into consideration in the analysis portion of this paper (Chapter 4.)

A few basic processes such as multiple scattering and ionization were also included for muons and protons (see Ref. [32]), but no hadronic interactions were considered for this background study. As of this publication, Geant4 has no functionality for lepto-nucleon or photo-nucleon interactions. Instead, these processes were designed by the user as primary events and will be covered in Section 4.5. Such a specific treatment of these interactions is justified by their rarity relative to the electro-magnetic processes. One additional, user defined, process was created with the sole purpose of killing any particle with less than 100 MeV of kinetic energy. This is justified because it speeds up the calculations greatly and 100 MeV is well below the threshold of the calorimeter.

4.4 Geometry

After defining the various materials, particle and processes, the next step in creating this simulation was to reproduce the experimental setup as completely as possible in the Geant4 environment. Due to the speed of modern computers it was possible mimic the intricate design of our target housing, magnet and insert without worrying about the extra computations this would require. As a result, the entire target refrigerator can and its contents were broken up into over 20 separate pieces, each made of an appropriate material. Figure 4.1 shows a top-view of the refrigerator can and its contents.

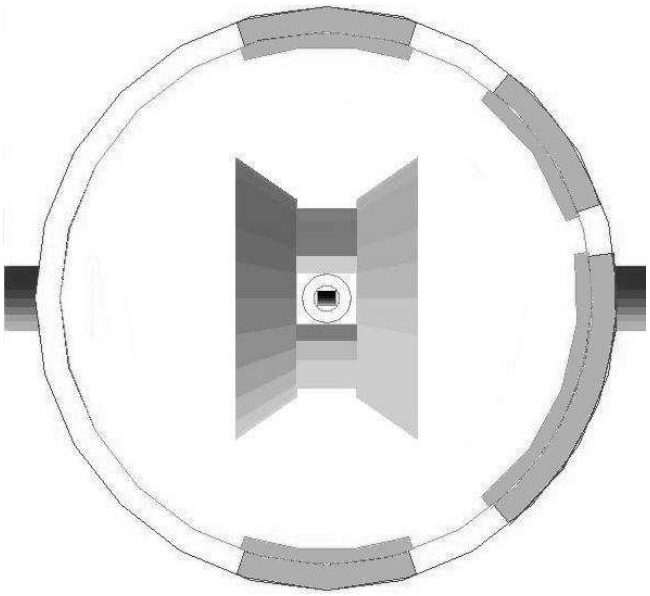

Figure 4.1: *A wire-frame rendering of the target refrigerator can (outer circle) and the 77K shield (inner circle) as seen from above. The target magnet (two wedges) and the target cell (small object at center) can be seen as solid objects. Edges of the upstream and downstream beampipes can be seen on the far left and far right, respectively. The shaded areas mark the extent of the four thin windows.*

During the process of creating this simulation the radiator took many different shapes and was placed in many different locations in an attempt to find an ideal orientation and distance from the target cell. The final setup was a thin cylinder located outside the target refrigerator can, about 10 cm upstream of the refrigerator can wall. It was given the physical properties of copper and a thickness of 10 percent of the copper radiation length, or 0.143 cm.

Since this simulation does not attempt to mimic the response of the calorimeter or the HMS, these two detectors were each treated as simple windows designed to record the data for any particle that passed through. They were also designed to immediately kill any incident particle in order to eliminate the possibility of multiple detections

and to reduce tracking time. The simulated calorimeter was a thin rectangular sheet with the total dimensions of the Pb-glass bars given in Figure 3.4. For the backward scattering orientation, it was placed 2.5 m away from the target at an angle of 82 degrees. The HMS was represented as a similar thin rectangular sheet of vertical height 165.4 cm and horizontal length 44 cm. It was placed 1 m away from the target to mimic the appropriate solid angle of the real spectrometer, which is ± 86.5 mrad by ± 22 mrad [39]. Again, the simulated HMS was designed solely to record the data of every incident particle and then immediately kill those particles.

The target outer vacuum can itself was constructed of aluminum and given a hollow cylindrical shape of inner radius 45.60 cm and height 77.47 cm. Four holes were then carved out of this can by subtracting appropriate cylinder sections from the can. Thin cylindrical sections were then placed over the holes and logically unioned to the can to create the windows. The thickness of the windows was 0.013 inches, while the thickness of the rest of the can was set to 0.935 inches. A hole of radius 2.00 inches was also carved out of the can on the upstream beamline to make way for the beryllium window. The interior of the hollow target refrigerator can was then given the properties of vacuum. The beam window was constructed of beryllium and had a thickness of 0.02 inches. The small posts connecting the refrigerator can to the LN2 shield at the windows and the vacuum openings were excluded from the simulation.

The liquid nitrogen shield was then created in a similar way. Unfortunately, the plans for the nitrogen shield had not been finalized at the time of this simulation, so some of the dimensions and thicknesses are only estimates. The height of this cylinder was 78.74 cm and the inner radius was 41.50 cm. The thickness of the 77K shield windows was 0.002 inches and the thickness of the shield itself was set to 0.935 inches. This over-estimates the actual shield thickness by about a factor of 4. The vast majority of particles travel through the windows, though, so this error had a

negligible effect on the simulation. The beam window for the LN2 shield had a radius of 2.25 inches and a thickness of 0.013 inches. It was made of beryllium as well. This is not an accurate representation of the actual 77 K shield window, which will be a thin sheet of mylar. This minor error did not affect the data, though, as the incident beam was simulated separately from the photo- and lepton- nucleon events. In both the refrigerator can and LN2 shield one of the larger aluminum windows overlaps the beam exit, so no additional window is needed on the downstream beam line.

The polarized target magnet was formed from two identical conic sections of the appropriate dimensions. These pieces were then connected with equally spaced sections of a cylinder of radius 10 cm. This design creates 6 openings in the magnet. The two along the beamline are conical in shape with an opening angle of 50 deg. The other four openings are wedge shaped and centered along the $\pm$x and $\pm$y axes. These have opening angles of 34 deg. For this experiment the target will be polarized parallel to the beam direction, so the magnet was oriented with the bore parallel to the beamline. The magnet and braces were both considered to be constructed of niobium since the actual composition was much too complicated to be taken into account. The target magnet field, itself, was treated as a separate entity attached to the world volume, at the origin. The field values were read in directly from a field map file [40].

The target area of the refrigerator can consisted of a 4 K liquid helium shield, a nosepiece, the target cell wall and the target material itself. The helium shield was an aluminum cylinder of height 78.74 cm, inner radius 4 cm and thickness 0.00381 cm. It was oriented with its axis in the vertical direction and was filled with vacuum. The nosepiece was another aluminum cylinder, interior to the 4 K helium shield, with the same height, inner radius 2.1 cm and thickness 0.00254 cm. The nosepiece was filled with 4 K liquid helium. The cell wall was located inside the nosepiece and on

the beam line. It was a cylinder of radius 1.25 cm, length 3 cm and thickness 0.0127 cm. The cell wall was also made of aluminum and was filled with a user defined material called "TargetNH3." Refer to Section 2 of this chapter for more details. Table 4.1 lists every object through which the beam passes along with the thickness, density and z-coordinate of each object. The data given here is the same as that used in the simulation and may not be consistent with the most recent version of the experimental design.

Table 4.1: *A list of every object through which the beam passes. This data is only for this simulation and may not be consistent with the most recent incarnation of the experimental design. z is the distance from the target center to the center of the object along the beamline. d is the thickness of the object.*

Object	Material	z (cm)	d (mm)	density ($\frac{g}{cm^3}$)
Radiator	Cu	-60.00	1.43	8.96
OVC	Be	-45.61	0.33	1.85
77K shield	Be	-41.51	0.330	1.85
He shield	Al	-4.00	0.038	2.70
Nose	Al	-2.10	0.051	2.70
1K He	Liquid He	-1.80	6.00	0.125
Cell Wall	Al	-1.5	0.127	2.70
Target	NH_3 & He	0.00	15.0	0.50
Cell Wall	Al	1.5	0.127	2.70
1K He	Liquid He	1.80	6.00	0.125
Nose	Al	2.10	0.051	2.70
He shield	Al	4.00	0.038	2.70
77K shield	Be	41.51	0.330	1.85
OVC	Be	45.61	0.33	1.85

Evacuated beam pipes were also included in this simulation mainly to see what effects they would have on the electromagnetic backgrounds. As the electron beam passes through the radiator and the target refrigerator can it gets spread out in the off axis directions and could conceivably splash along the beam pipe and shower into the calorimeter. The exact dimensions on the beam pipes that will be used in

this experiment are not yet known to the author, so the dimensions were guessed at based on schematic diagrams of Hall C. These proxies should be similar enough to the real beam pipes to make accurate background predictions. The upstream and downstream beam pipes each were made of two sections. The sections nearest the target refrigerator can had an inner radius of 2 inches and a thickness of 0.125 inches. The sections further upstream and downstream from the refrigerator can had an inner radius of 4 inches and a thickness of 0.250 inches. The smaller sections were both about 5 m long and the larger section were both about 12 m long. All parts of the beam pipe were given the properties of aluminum and the cavities were given the properties of vacuum. A thin cylinder was also placed perpendicular to the beam line at the end of the last downstream beam pipe. It was designed to act as a detector for any particles entering the beam dump. It should also be noted that the radiator mentioned above must necessarily be placed as a daughter volume of the upstream beam pipe. Lastly, the dimensions and densities used to construct this geometry may become obsolete as the experimental design changes and the real objects are built.

4.5 Event Generation

Geant4 is an ideal environment for investigating the electromagnetic backgrounds of any experiment because of the great deal of work that has been put into this area. A primary event generator exists which allows the definition of any number of primary event particles with any desired momenta and in any desired state. Once this is done, the primary event generator will be called at the beginning of each event and it will create exactly one set of these particles. The primary particles are then turned over to the tracking manager and treated just like any other particle in the simulation. An example of an electromagnetic shower can be seen in Figure 4.2. Simulation

setups such as this can be used to examine the electromagnetic background at the calorimeter and to determine where shielding should be placed.

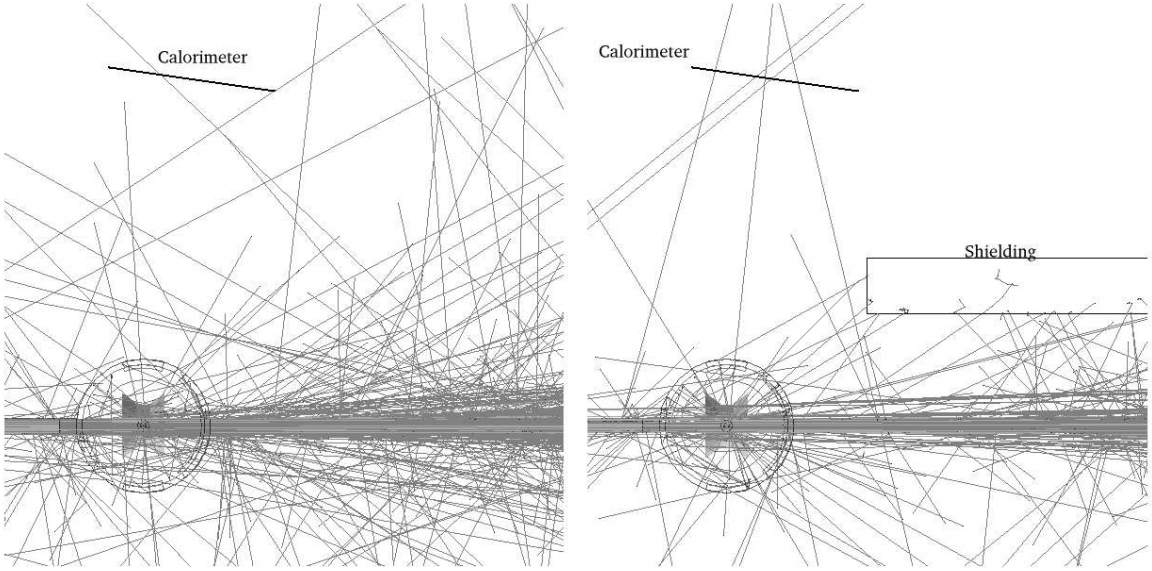

Figure 4.2: *An example of an electromagnetic shower using the WACS simulation setup and a simple electron beam. The left image is for the case where no shielding is used and the right image is for the case where shielding has been placed parallel to the downstream beam pipe. In each image the beam particles move left to right and 1000 primary 4.8 GeV electrons were used. All visible tracks represent particles with energy of at least 200 MeV.*

In order to investigate the electromagnetic background, an electron beam of energy 4.8 GeV was created about 20 meters upstream of the target cell and given a momentum direction along the positive z axis. The initial x and y coordinates of the particles were randomized over a radius of 1 cm to simulate the slow raster which is ensures the entire target sample receives an equal dose of beam. This electron beam was used in the early stages of the simulation to do the following:

1. Test the electromagnetic processes.

2. Test the simulation's data acquisition system.

3. Generate the bremsstrahlung spectrum needed for data analysis (see Figure 3.2.)

4. Compare various radiator placements.

The actual non-electromagnetic background for this experiment was much more difficult to generate because photo-nucleon and lepto-nucleon interactions had not yet been implemented in the Geant4 toolkit. The framework for such events did exist, but it was ignored due to the small cross sections involved and the fact that only a small kinematics range was of interest. Instead of developing a physical process similar to the existing bremsstrahlung or ionization code, it was decided to treat these photo-nucleon and lepto-nucleon events as primary events. Instead of tracking an electron or photon to the target cell, a final state photon, electron or pion was generated within the target cell along with the recoil proton. The initial location of the scattering event was randomized over the entire target cell and the final momentum direction of the scattered particle was randomized over the solid angle subtended by the HMS opening. This information, combined with a randomly generated initial beam particle energy allows the calculation of all other necessary momenta and directions. And by requiring the proton to go in the direction of the HMS it was ensured that computer time was only used on interesting events. Naturally, this produced an even distribution of events across the full energy range.

The three processes that were studied in this way were Compton scattering from the proton, elastic electron scattering from the proton and photo production of neutral pions from the proton. In each case, the kinematics are that of a simple two body interaction. Motion of the beam particle perpendicular to the z axis was ignored, but the Fermi motion of the target protons was taken into account. The initial (Fermi) momentum of the target proton was set by first determining the type of proton

involved. Approximately 29% of the target protons exist as nearly free Hydrogen atoms and have no initial momentum. Another ~68% of the protons are bound in Nitrogen and the remaining ~3% are bound in liquid Helium. These bound nucleons were given initial momenta flatly distributed from 0 to some maximum value and randomized over all directions. The maximum value for Nitrogen (220 MeV/c) was taken from Reference [41], while the maximum value for Helium was estimated at 70 MeV/c. This underestimates the actual Fermi momentum of Helium-4 by nearly a factor of 2. Given the initial state of the proton target and the beam particle, as well as the final momentum direction of the recoil proton, it is possible to reconstruct the entire interaction. The code used to do this can be found at

`http://spin.phys.virginia.edu/jlw9p`,

but a description of the kinematical calculations follows.

4.6 Kinematics

First, the known quantities must be defined. The initial momentum of the incident photon or electron is defined as p_1. Then the direction of the final state photon, electron, or pion is randomly generated over the solid angle subtended by the calorimeter;

$$\hat{p}_3 = \left(\frac{p_{3x}}{|\vec{p}|}, \frac{p_{3y}}{|\vec{p}|}, \frac{p_{3z}}{|\vec{p}|} \right). \tag{4.6}$$

After that, the initial state of the target proton

$$p_2 = (\sqrt{M_p^2 + |p_2|^2}, p_{2x}, p_{2y}, p_{2z}), \tag{4.7}$$

where $|p2|$ is given by the distributions described in Chapter 5, Section 1 and M_p is the rest mass of a proton. Now that the initial conditions have been set and the final state has been uniquely sampled it is possible to calculate all of the remaining kinematics variables. Conservation of 3-momentum can be used to determine p_4^2 (the recoil proton momentum) in terms of p_3^2. This can then be used with conservation of energy,

$$p_1 + \sqrt{M_p^2 + p_2^2} = \sqrt{M_s^2 + p_3^2} + \sqrt{M_p^2 + p_4^2}, \tag{4.8}$$

to determine $|p_3|$. Here M_s is zero in the case of elastic events or the mass of the neutral pion in the case of pi photo-production. Conservation of momentum can finally be reapplied to determine the exact 4-momentum of the recoil proton.

Six different runs were used to obtain the desired statistics. The first three runs generated 2.5 million primaries for each of the three non-electromagnetic processes with incident beam energies flatly distributed over the range $p1 \in$[1000,4800] MeV/c. This data was analyzed by applying a series of cuts, which will be described in the analysis chapter. It was noted that the only events to survive a very broad series of cuts were those with incident beam energies in the range $p1 \in$[3900,4700] MeV/c. This range is limited by the acceptance of the HMS. The second set of three runs generated 1 million events for each of the three non-electromagnetic processes with incident beam energies flatly distributed over this new, narrower range. Narrowing the energy range in this way increased the rate at which useful data was obtained, without sacrificing any of the experiment's phase space.

4.7 Tracking

After the primary event generator creates a particle or set of particles, they are passed on to the event manager which controls the overall flow of the tracking phase. The event manager then passes these particle down to the tracking manager. The tracking manager then steps the particles through the geometry of the simulation, implementing electromagnetic and decay processes as necessary. When new particles are created, they are passed along to the event manager for storage until the event manager is ready to have them tracked as well. Killed particles are removed from the event manager's stack entirely and their total energy is recorded as having been deposited in the material.

The probability of a given process occurring during a given step is determined by the mean free path of the process [32]

$$\lambda(E) = \left(\sum_i [n_i \cdot \sigma(Z_i, E)] \right)^{-1}, \tag{4.9}$$

where n_i is the number of atoms per unit volume of the i^{th} element, $\sigma(Z, E)$ is the total cross section per atom and the sum runs over all of the elements in the material through which the particle is traveling. At the beginning of each run, the cross sections and mean free paths are calculated and stored in memory for every combination of process, particle and material. Then, during the tracking process, the interaction point for a given process is determined by sampling the number of mean free paths the particle will traverse as $n_\lambda = -log(\eta)$, where η is a random number in (0,1). The number of mean free paths is updated after each step a particle takes until the step originating from this process is the shortest. It is at this time that the given process occurs. When a process occurs, the kinematical quantities are calculated as described

above and particles are created and destroyed accordingly. Often, the process with the shortest step size is the transportation process because this process automatically takes a step length equal to what is needed to propagate the particle into a new material. Once in the new material the mean free path for each process changes and the procedure start over again.

4.8 Data Acquisition

The data acquisition part of the simulation was designed to be both efficient and effective. While it is possible to record every step that every particle takes through the simulator, this would require a significant increase in the number of computations and would add greatly to the computing time. Instead, only the steps of interest were recorded. While studying the electromagnetic background, all particles reaching the target cell, the beam dump, the calorimeter and the HMS were recorded. This information allowed the calculation of the total power that would be reaching each of these objects under actual experimental conditions (i.e. a 90 nA beam of 4.8 GeV electrons.) While examining the non-electromagnetic backgrounds the initial state of the two primary particles was recorded along with the state of every particle to reach the HMS and the calorimeter. In this case, though, only particles with kinetic energy over 100 MeV were kept. All lower energy particles would be under the threshold of either detector.

Each step was recorded as an n-tuple for the ROOT analysis toolkit [42]. This toolkit is ideal for analyzing large amounts of data. Since both Geant4 and the ROOT analysis toolkit are maintained by CERN, there does exist some cross functionality. That is to say, it is possible to run Geant4 from within ROOT or to build ROOT n-tuples directly in Geant4. Do to some difficulties with this functionality, this simu-

lation built the n-tuples via a more indirect route. First the data was output as text and then the text was then immediately used to fill ROOT trees. This procedure required very little overhead, but it would still be useful to build the trees directly in Geant4 in the future.

Chapter 5

Analysis and Results

The goal of this simulation was to generate, as accurately as possible, the non-electromagnetic events that will dominate in the future Compton experiment. In order to do this, the following three processes had to be simulated for both free protons and those bound in nucleons:

1. Real Compton scattering from the proton.
2. Elastic electron scattering from the proton.
3. Neutral pion photo-production on the proton.

For each of these processes three variables had to be sampled;

1. The incident beam particle momentum.
2. The Fermi momentum of the target proton.
3. The scattering angle of the recoil proton.

In order for the simulation to accurately portray reality, each variable in the phase space had be sampled according to an appropriate distribution function. There are

two main schools of thought on how to achieve this. The first method is to weight the events as they are sampled, while the second method is to sample the entire phase space equally and apply the weighting function after the simulation has run. Each method has its strengths and weaknesses, which will not be discussed here. This simulation used a combination of these two methods.

5.1 Sampling the Initial State

The Fermi momentum was weighted during the sampling process because the entire range of possible Fermi momenta was expected to result in "good" events. Also, it is very simple to approximate the Fermi momentum of a bound nucleon. While a realistic momentum distribution in heavy nuclei is broad peak with a sharp drop-off and a long tail, at high momentum it is safe to approximate this with a flat distribution extending out to some maximum value. This value varies as a function of the atomic number and for Nitrogen this simulation used the parameters found in Ref. [41]. Another consideration when dealing with the Fermi momentum is that there are three sources of protons from within the target cell. Each helium atom has two protons, and the maximum Fermi momentum was estimated at 70 MeV/c. As mentioned before, this underestimates the Fermi momentum of Helium-4 by almost a factor of 2. Each ammonia molecule, on the other hand, has three free protons that are at rest and seven nitrogen-bound protons with a maximum momentum of 220 MeV/c. Given a packing fraction of 50% and using the densities of solid ammonia and liquid helium it can be shown that the total number of protons in the target cell is divided into these proportions; 3% bound in helium, 29% free and 68% bound in nitrogen. Since this is a beam-target asymmetry experiment, we are only interested in taking data from protons that can be polarized (to first order, the free

ones.) The remainder of the target protons only contribute to the background and serve to increase the dilution factor.

The incident beam energy portion of the phase space was handled using the second of the two methods described above. For the first set of runs, the incident beam energy was sampled evenly over the range P1 = [1000 MeV, 4800MeV]. This range was then narrowed down to P1 = [3900 MeV, 4700MeV], once it was realized that only this energy range contributed to the signal. Figure 5.1 shows the incident beam (electrons and photons) energy for every event that resulted in a coincidence between the HMS and the Calorimeter. This range is defined by the acceptance of the HMS.

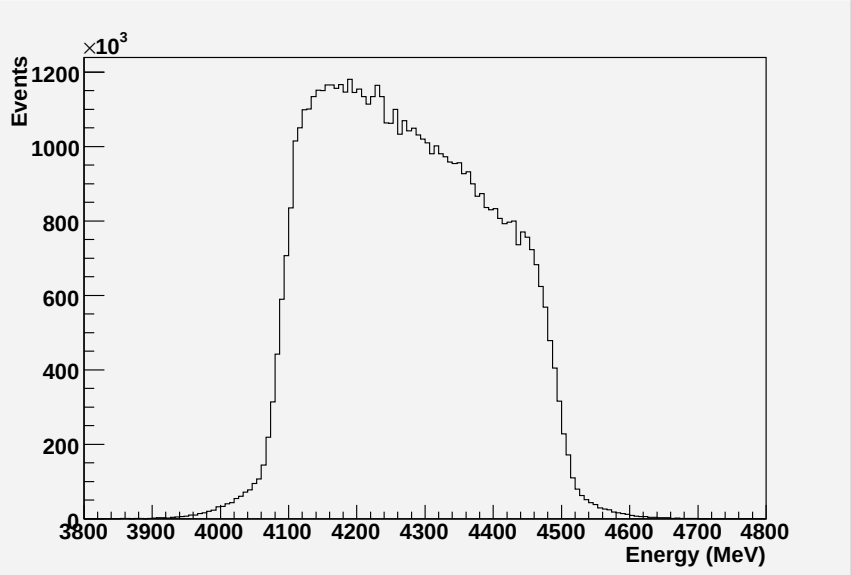

Figure 5.1: *The range of incident particle energy that resulted in coincidence events that survived every necessary cut. This is the range of incident particle energies that contribute to the signal.*

The flat distribution of the incident beam energy then needed to be weighted by an appropriate distribution function, namely the energy spectrum of the bremsstrahlung beam. Naturally, the elastic electron scattering events were weighted with the post bremsstrahlung electron spectrum and the Compton and neutral pion photo-production events were weighted with the bremsstrahlung photon spectrum. These spectra can

be seen in Figure 3.2. Each spectrum was first parameterized with a function of the form;

$$W = a_0 + e^{a_1 + a_2 P_1} + e^{a_3 + a_4 P_1}, \tag{5.1}$$

where the a_i's are constants and P_1 is the incident beam energy. The photon spectrum was fit over the interval $\in$[1000,4800] MeV. The electron spectrum, however, was only fit over the interval $\in$[1000,4500] MeV due to the sharp peak near the endpoint. Weights for the range $\in$[4500,4800] were extracted directly from a data table, rather than from a parameterisation. These weights were applied during data analysis.

5.2 Sampling the Final State

The most difficult variables to sample were the azimuthal and polar scattering angles of the recoil proton. These had to be sampled over a region slightly larger than the solid angle subtended by the HMS. This was done by sampling the 3-vector of the recoil proton momentum direction over the entire face of the HMS. Ideally, one would sample the azimuthal and polar angles directly, but this approximation is valid due to the small size of the HMS relative to its distance from the target center. A simple correction could be applied by weighting events by a factor of

$$W_{HMS} = \frac{D_0}{\sqrt{D_0^2 + d^2}}, \tag{5.2}$$

where D_0 is the distance between the center of the target and the center of the HMS and d is the displacement of the proton detection point in the HMS coordinate frame ($d = \sqrt{X_{HMS}^2 + Y_{HMS}^2}$.) Within the small angle approximation, this factor is unity over the entire HMS spatial acceptance.

The final state of the interaction is then weighted by the cross section for the

appropriate process. It was most convenient to use the differential cross section with respect to Mandeslstam t. For elastic electron scattering, the equivalent of the Rosenbluth formula [43] was used:

$$\frac{d\sigma}{d(-t)} = \frac{4\pi\alpha^2}{t^2}\left(1 + \frac{t}{\hat{s}} + \frac{tM_p^2}{\hat{s}^2}\right)\left[\frac{G_E^2 + \tau G_M^2}{1+\tau} + \frac{G_M^2 t^2}{2\hat{s}(\hat{s}+t) + 2tM_p^2}\right], \tag{5.3}$$

where $\hat{s} = s^2 - M_p^2$, $\tau = q^2/2M_p^2$ and G_E and G_M are the electric and magnetic form factors of the proton, respectively. This simulation used a parameterization of the elastic form factors from Ref. [44]. This parameterization fits the wide range of existing proton form factor data taken from electron scattering experiments.

Cross sections for real Compton scattering and neutral pion photo-production are not so readily available and, as mentioned before, only two major experiments have so far endeavored to measure these cross sections at backward angles. A crude scaling law fit to the Cornell data [22] was used for each process. So, the Compton events were weighted with factors of

$$\frac{d\sigma}{dt} = \frac{30\,\mu\mathrm{b\,GeV}^{10}}{s^6} \tag{5.4}$$

and the neutral pion production events were weighted with a factor of

$$\frac{d\sigma}{dt} = \frac{20\,\mathrm{mb\,GeV}^{12}}{s^7}. \tag{5.5}$$

Since this simulation operates around $s = 9$ GeV^2, the weighting for the pion photo-production events is about two orders of magnitude higher than that for the Compton events.

Weighting of the final state does not stop with the cross sections, though. There are two processes not included in Geant4 that serve to preferentially attenuate the

pion coincidences. These processes are hadronic in nature and only affect pions and recoil protons [45]. The first is an inelastic interaction that amounts to re-absorption of the hadron and can be accounted for by a transparency factor. Transparency experiments for Carbon, which we take for Nitrogen, indicate that T_p=0.55 and T_π=0.6 [28]. That is to say, 55% of all recoil protons and 60% of neutral pions will actually make it out of the nucleus that spawned them. The second of these coincidence attenuating processes is re-scattering in the nucleus that leads to a loss in the kinematic correlation between the recoil proton and the scattered particle or produced pion. This process is accounted for by applying an additional weight of 0.5 to each recoil proton and photo-produced pion [45]. These two processes preferentially attentuate the pion signal because only the pion events have two hadrons in the final state.

5.3 Event Reconstruction

During a simulation run, only the events that involve a coincidence between the HMS and the calorimeter are recorded. For these events, the simulation provides every piece of information desired, including the state of each scattered and recoil particle in the nucleus. An initial cut is applied by the data acquisition process. Only the events that involve a coincidence between the HMS and the calorimeter are recorded. When the actual experiment is run, much of this data won't be available, though. Instead it will have to be reconstructed from the state of the recoil proton in the spectrometer. If we treat the HMS as a simple plane detector, then it is possible to reconstruct the event based solely on three pieces of information:

1. The momentum of the proton at the HMS.

2. The point at which the proton strikes is detected in the HMS.

3. The location of the beam raster (in the plane perpendicular to the beam direction.

First it is necessary to define the coordinate systems that will be used herein. It has already been noted that the target reference frame is such that the $+z$ axis points in the direction the beam travels. The +y axis is vertically upward and the $+x$ axis is given by the right hand rule. The HMS reference frame is defined such that the $+z^{\star}$ axis is normal to the surface of the HMS and pointed away from the target center, while the $+x^{\star}$ axis points vertically upward. Similarly, the calorimeter reference frame is defined so that the $+z^{\bullet}$ axis is normal to the calorimeter surface and pointed away from the target center. It was then convenient to make the $+x^{\bullet}$ axis point the same direction as the.$+x^{\star}$ axis.

In order to reconstruct the interaction we start with the momentum of the proton at the HMS, $(P_x^{\star}, P_y^{\star}, P_z^{\star})$, and the location at which it struck the HMS, $(X^{\star}, Y^{\star})$, both in the HMS frame. This momentum differs only slightly from the momentum of the proton at the interaction vertex inside the target cell. The change in momentum direction is caused by the target magnetic field and, to a lesser degree, by scattering from material in the target can. This change was accounted for by plotting (Figure 5.2) the difference between the momentum at the HMS and the momentum at the interaction vertex for a large number of events. The mean of this difference was then added to the momentum at the HMS, thus shifting the momentum back to the value it had at the interaction vertex. A more accurate method would be to track each proton back to the target cell using a ray tracing program. Once the momentum of the recoil proton at the interaction vertex is known it is possible to calculate the incident beam energy and scattered photon 4-momentum using conservation of momentum and energy.

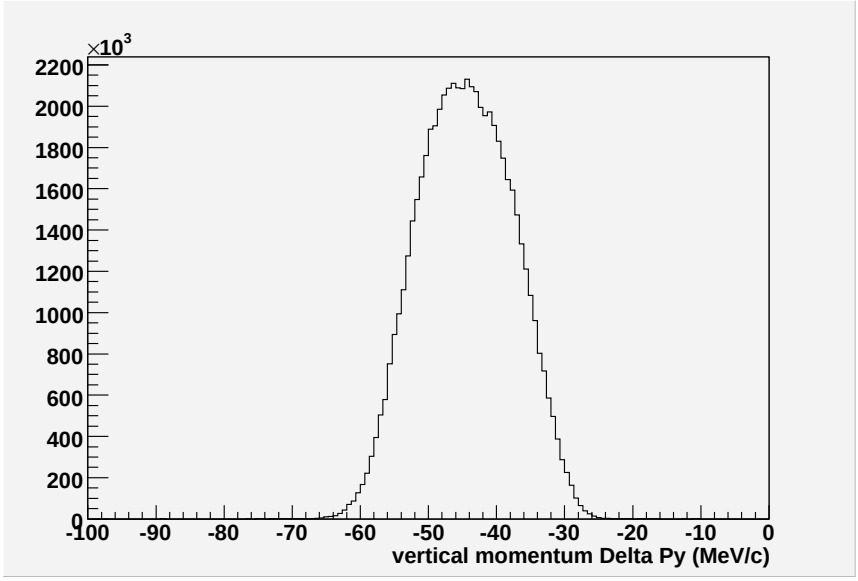

Figure 5.2: *The event distribution for the difference $P_y^{target} - P_y^{HMS}$ in the vertical component of the proton momentum. P_y^{target} is the value at the interaction vertex. P_y^{HMS} is the value at the HMS detector plane. The increase in this component of momentum is caused by the target magnet's field. A much smaller shift is seen in the other two components of the proton momentum to compensate.*

The next step is to reconstruct the exact location of the interaction vertex within the target cell, $r(X_v, Y_v, Z_v)$. X_v and Y_v are both determined by the raster position of the beam. The z component is determined from the HMS data and is calculated as

$$Z_v = \frac{RD - Y^\star - X_v \cos\theta_{HMS}}{\sin\theta_{HMS} + R\sec\theta_{HMS}}, \tag{5.6}$$

where θ_{HMS} is the HMS angle setting, D is the distance from the target center to the center of the surface representing the HMS, $Y^\star$ is the horizontal component of the location that the proton struck the HMS, and $R = P_y^\star / P_z^\star$. $P_i^\star$ is the i^{th} component of the proton momentum in the HMS frame. Now that the location of the interaction vertex has been determined, it is trivial to calculate the distance from this point to the calorimeter plane, D_{CAL} and the horizontal distance from this point to the line that runs through the center of the target cell and the center of the calorimeter, $d_y^\bullet$.

Using these quantities we can then predict the location at which the scattered photon will strike the calorimeter, $(X^\bullet, Y^\bullet)$, in the calorimeter frame;

$$X^\bullet = Y_v + D_{CAL}\frac{k_x^\bullet}{k_z^\bullet}, \qquad\qquad Y^\bullet = d_y^\bullet + D_{CAL}\frac{k_y^\bullet}{k_z^\bullet}. \tag{5.7}$$

Here, $k_i^\bullet$ is the i^{th} component of the photon momentum in the calorimeter frame. Now that we have the predicted location of the photon detection, it can be compared with the actual measured location. It will be useful to define the horizontal and vertical correlation parameters for the calorimeter;

$$\delta Y = Y^\star - Y_r^\star \qquad \text{(horizontal)}, \tag{5.8}$$

$$\delta X = X^\star - X_r^\star \qquad \text{(vertical)}, \tag{5.9}$$

where the subscript r indicates the variable was reconstructed from the HMS data.

5.4 Results and Conclusions

The raw data sets contain information for every event in which both the calorimeter and the HMS detected at least one particle. Since the ultimate goal of the experiment will be to examine Compton scattering from free protons, much of the raw data must be cut away. A series of cuts on energy, position and angle were devised to do just this. For the backward angle:

1. A cut on the momentum of the proton. It was designed to match the acceptance of the HMS, which is $\pm$ 8% the central momentum. In this case, the central momentum will be set for 4250 MeV, which corresponds to a kinetic energy of 3410 MeV. As a result, the cut on the kinetic energy is $\pm$ 340 MeV. This cut

serves to eliminate all events in which the proton enters the HMS window but does not make it into the detector hut.

2. A cut on the energy of the photon. The cut on the proton kinetic energy severely restricts the range of photon energies, but a cut here is still necessary. The photon must be within 150 MeV of the central photon energy of 870 MeV. This serves to eliminate most events in which two or more particles struck the calorimeter in coincidence with a single proton.

3. A cut on the reconstructed incident beam particle energy. This cut is necessary to ensure that events from the bremsstrahlung endpoint are not included. Near the endpoint, the ratio of electrons to photons in the incident beam rapidly increases. A cut of 4300 MeV $\pm$ 200 MeV will eliminate most of these unwanted electrons and, conequently, many of the unwanted ep$\rightarrow$ epγ events.

4. A cut on the horizontal correlation parameter δY, as defined in the previous section. A suitable cut must be applied here in order to properly view the vertical correlation parameter, δX. Essentially, this cuts off the wings of the broad pion background and prevents them from artificially inflating the pion background in a 1-D vertical correlation plot. Nearly all of the good real Compton events lie within $\pm$ 150 mm of the origin.

5. A coplanarity cut. This cut is powerful, but tends to eliminate many events that are also eliminated by other cuts. It is the difference between the reconstructed polar angle of the recoil proton and the polar angle of the scattered particle. There are only two ways that a given event can appear to be non-copolanar and still satisfy the requirement of causing a coincidence between the HMS and the calorimeter. The first is if the target proton was bound in a nucleus and had

a substantial amount of Fermi momentum perpendicular to the z axis. In this case, the event was truly not coplanar in the lab frame. The second is if the scattered particle was an electron. When the electrons are bent vertically by the target magnet, this amounts to a change in their measured polar and azimuthal angles. Thus, all elastic ep events will appear to be non-coplanar, except those in which the electron emits a hard bremsstralung photon immediately after scattering. By cutting sharply around zero (± 2 degrees), all elastic ep events and many events involving a bound target proton will be removed.

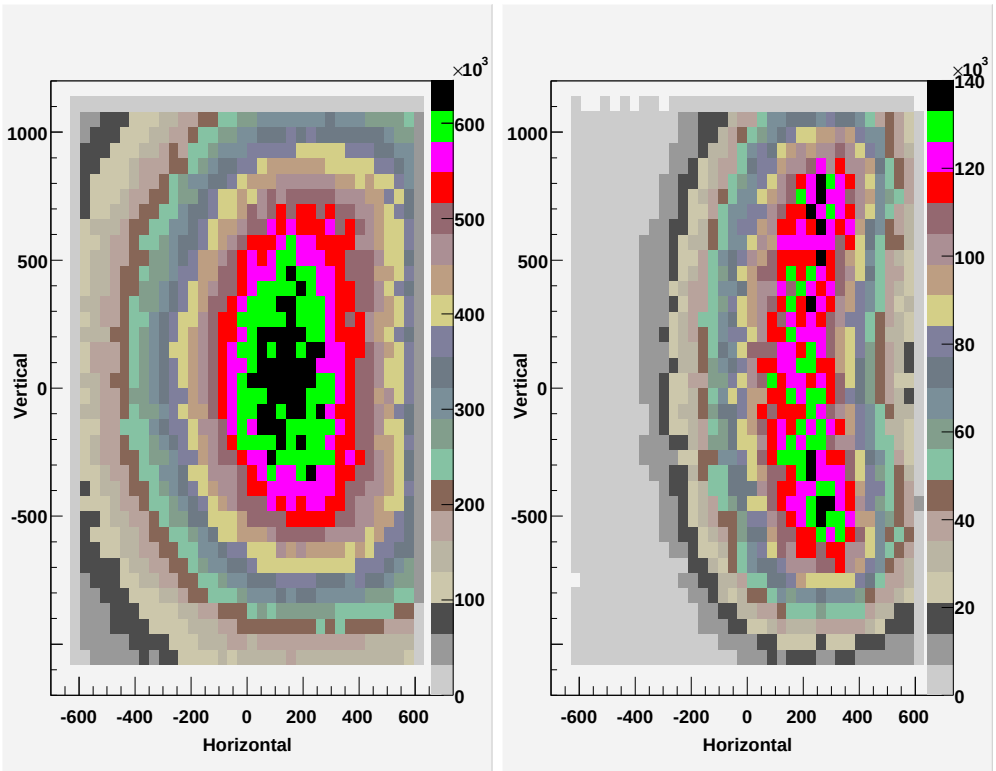

Figure 5.3: *Event distribution in the calorimeter. The x axis is the horizontal calorimeter dimension and the y axis is the vertical. The left image is after only applying the cut on the proton momentum. The right image is after also applying a cut on the calorimeter energy and on the reconstructed incident beam energy. The arc in the right image coincides with the central scattering angle of the experiment, 82 degrees.*

The cuts mentioned above, particularly the first three, exclude a great deal of the raw data and reveal the actual signals of interest. Figure 5.3 shows the event distribution in the calorimeter. After the cuts are applied an arc of data is left centered near the central scattering angle in which we are interested, 82 degrees. This is not very useful for particle identification, though. Instead, it is better to look at the correlation parameters defined in the previous section. Figure 5.4 shows the vertical correlation parameter (δX) and Figure 5.5 shows the horizontal correlation parameter (δY), both before and after cuts. The second and third cut mentioned above clearly reveal the sharp Compton peak on top of the broad pion background. This effect is more clear in the vertical direction as a result of the event reconstruction process. Essentially, the error in the z component of the interaction vertex translates into an error in the scattering angle of the Compton photon. At the calorimeter, this error is seen as a smearing out of the Compton peak preferentially in the horizontal direction. As a result, a horizontal slice through the Compton peak will have an elliptical cross section, rather than circular.

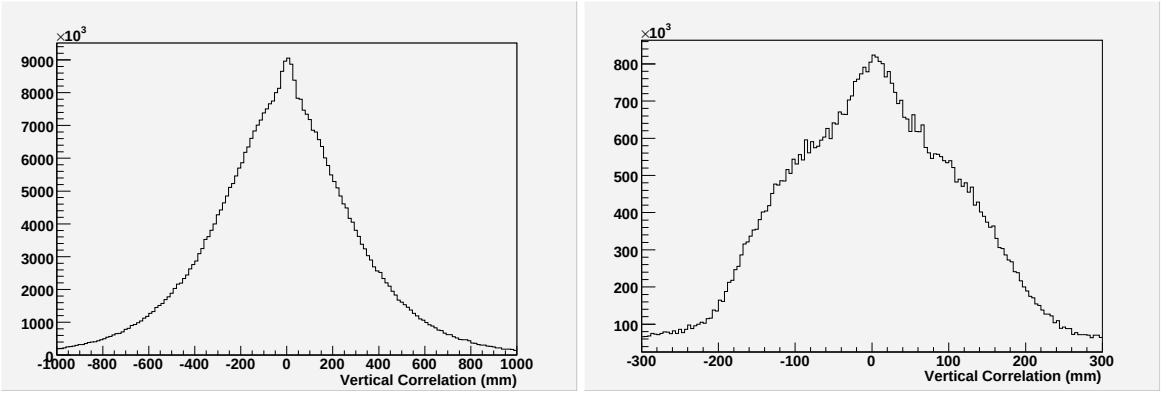

Figure 5.4: *Event distribution versus the vertical correlation parameter (δX) in the calorimeter. The left image contains only a cut on the proton momentum. The right image contains this cut as well as a cut on the calorimeter energy and a cut on the reconstructed incident beam energy.*

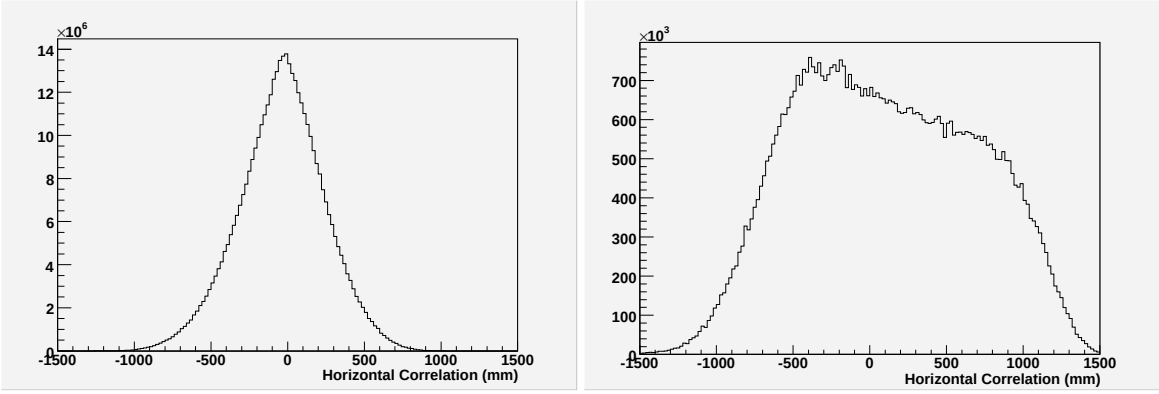

Figure 5.5: *Event distribution versus the horizontal correlation parameter (δY) in the calorimeter. The left image contains only a cut on the proton momentum. The right image contains this cut as well as a cut on the calorimeter energy and a cut on the reconstructed incident beam energy. The smearing of the Cmopton peak is caused by the event reconstruction process.*

The previous two figures can be combined to give a two dimensional view of the event distribution in the calorimeter. Figure 5.6 shows the event distribution plotted against both the horizontal and the vertical correlation parameters in the calorimeter. The broad pion background centered at the origin is visible with a sharp Compton peak at its center. The peak near $\delta X = 66$ cm is the elastic electron peak. It has been artificially suppressed by a factor of about 40 so that the pion and Compton peaks are more easily visible. It is clear from this figure that there will be no problem distinguishing the Compton peak from the elastic electron peak. The elastic electron-proton event distribution does have a tail that extends down to the orgin and interferes slightly with the Compton and pion signals. Near the origin, though, this tail is composed entirely of bremsstrahlung photons created by the elastically scattered electron in the target cell. In the previous RCS experiment it was found that the ratio of these $ep \rightarrow ep\gamma$ events to true Compton events is only a few percent [10].

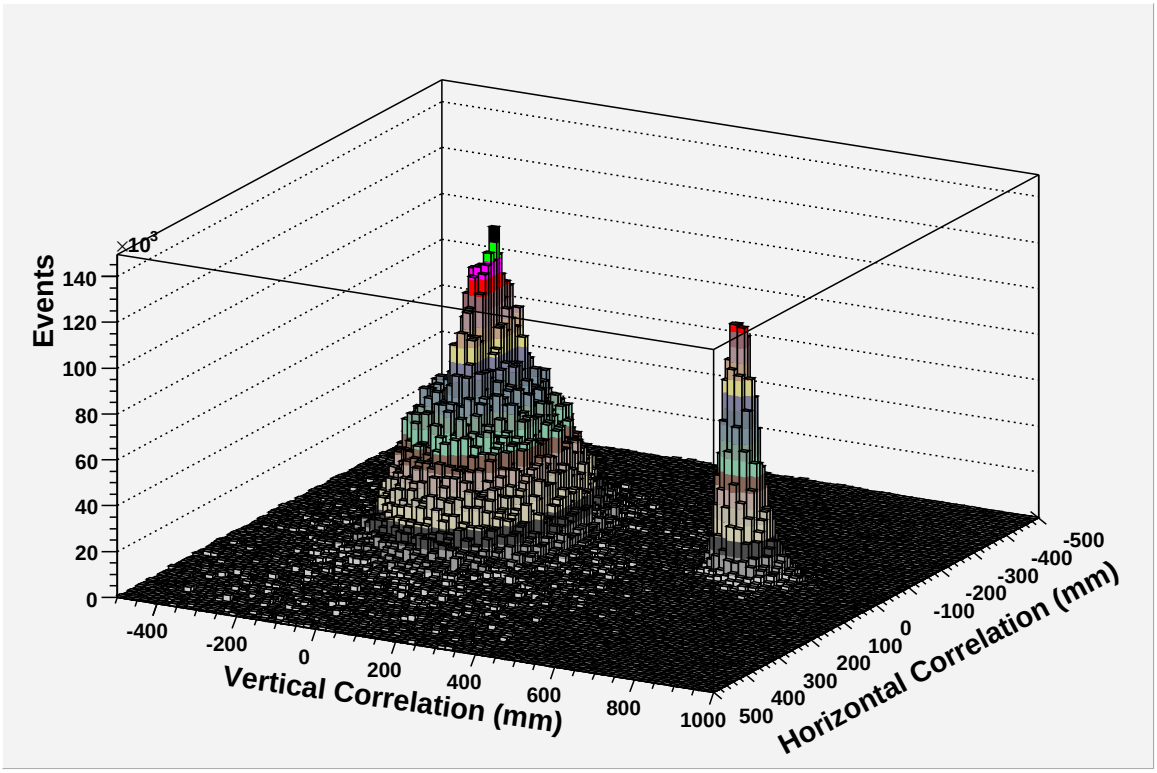

Figure 5.6: *Event distribution in the calorimeter versus the vertical and horizontal correlation parameters, δX and δY. The peak on the right is the elastic electron peak (reduced by a factor of 40), while the feature on the left is a sharp Compton scattering peak on top of a broad peak created by decaying neutral pions.*

Figure 5.7 shows δX with the first four cuts applied. Again, the Compton peak is clearly visible. The elastic electron events have been removed from this plot. During analysis of an actual experiment, in order to isolate the Compton peak the background would be fit on the range [-220,-50] and [50,220]. This fit would then be subtracted from Figure 5.7 to give the Compton signal. However, the Compton signal here can also be obtained directly from the simulation. The left image in Figure 5.8 gives the clean Compton signal for free protons with the first four cuts applied and the right image shows the background under the same conditions. Integrating the Compton peak on the range [-50,50] gives the number of Compton events in this bin, N_{RCS}. Integrating the background over the same range gives the number of non-Compton

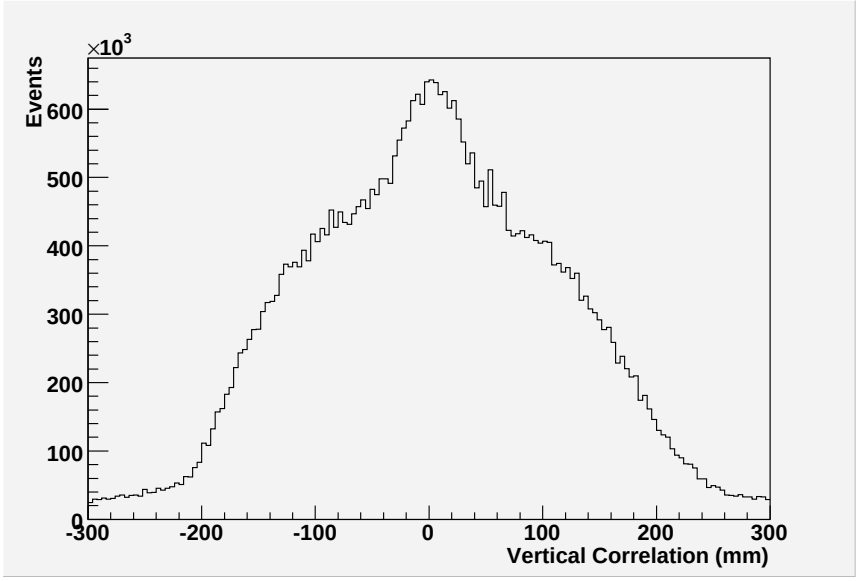

Figure 5.7: *Event distribution in the calorimeter versus the vertical correlation parameter for only the Compton and pion events. The Compton events form the sharp peak on top of the broader pion background.*

(background) events in this bin, N_b. From these the dilution factor is;

$$D = \frac{N_{RCS} + N_b}{N_b}. \tag{5.10}$$

For the backward scattering angle the dilution factor was calculated to be $D = 6.1$, in good agreement with previous estimates.

5.5 The Future

Though this simulation has come a long way, there is still a great deal of room for improvement. First of all, the following corrections will improve the accuracy of this simulation:

1. The cross sections can be improved. Currently, a simple scaling law fit to the Cornell data [22] is used for the Compton and pion photo-production cross

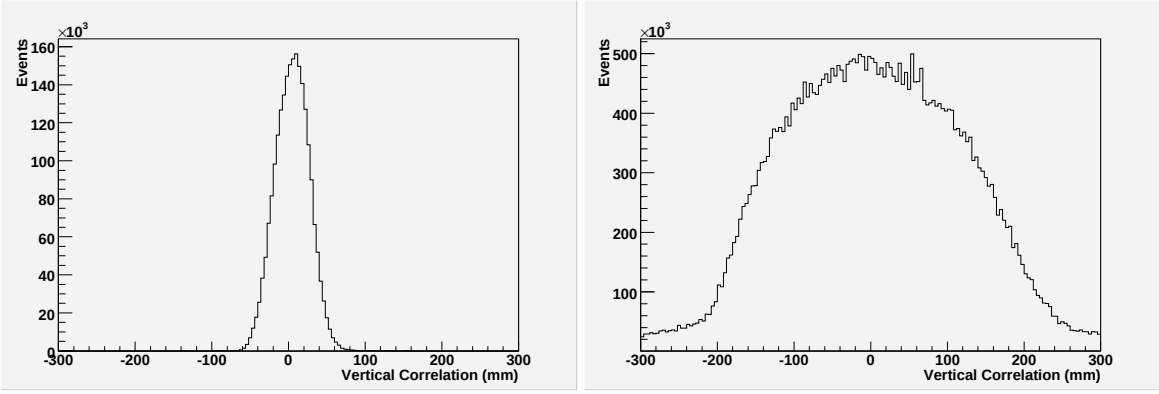

Figure 5.8: *Event distribution in the calorimeter versus the vertical correlation parameter. The left image shows only the Compton events that involved free protons. The right image shows pion background added to the background from Compton events that involved a bound nucleus. These were generated artificially, not by fitting the pion background and subtracting it from the total signal.*

section. Recent data from Hall A at Jefferson lab [46] can be used to better represent these cross sections at larger angles. Also, the elastic electron-proton scattering cross section should be tested more thoroughly.

2. The sampling of the final state is not yet ideal. Currently, the momentum direction of the recoil proton is sampled over the surface of the HMS detector plane. This is accurate to within the small angle approximation, but can be improved by calculating the actual solid angle that the HMS subtends. Then the events will be evenly dispersed over a sphere, as they should be.

3. The target composition can be more accurately portrayed. Currently, the packing fraction of the target cell is set to 50%, and the density of the target ammonia is set to 0.9 g/cm^3. In reality the packing fraction is closer to 60% and the target ammonia density differs slightly. Also, the density of 1 K Helium is 0.145 g/cm^3, significantly greater than that of 4 K Helium.

4. The dimensions of the 77K shield have been updated. The current thickness of the 77K shield and possibly the window thicknesses have changed since this simulation was created. Also, the beam window for the 77K shield is not properly represented in the simulation. Changing these dimensions will slightly alter the electromagnetic background in the simulation.

5. Standardize the reference frame. The simulation is written in a reference frame that is not the same as the target reference frame defined in this work. Instead, it has been rotated so that the x_s axis is in the direction of the beam, the z_s axis is vertically upward, and the y_s axis points toward the calorimeter. This coordinate system is a relic, and it should probably be changed in order to facilitate communication in the future.

6. Track protons back to target during analysis. Currently, the proton momentum at the interaction vertex is reconstructed in a rather crude manner. Actually tracking each individual proton back could improve the event reconstruction process.

7. Correct the ^{4}He Fermi momentum. Currently, the maximum value for Helium is set to 70 GeV/c. In reality, it is over 100 MeV/c. Also, the simulation currently weights the Helium events with the same transparency factor as the Nitrogen events. In reality, this factor is substantially larger for the smaller nucleus.

8. Change the material of the target cell wall. Currently, the target cell wall is made of aluminum. In reality the cell wall is made of Kel-F, which is less dense than aluminum.

There are also numerous additions that would benefit this simulation:

1. Fully integrate the root analysis toolkit. This is the most important addition that can be made from a logistical standpoint. There exists a way to integrate the root analysis software into the Geant4 toolkit, so that all data is printed directly to root trees. Completing the integration for this simulation would save the user a significant amount of time and effort in the long run.

2. Sample over the helium outside the target cell as well. Currently, events are only produced inside the target cell. But elastic and quasi-elastic events will also be taking place in the helium that is both up-stream and down-stream of the target cell. Since it is impossible to perfectly reconstruct the interaction vertex, some of these events will contaminate our data. The same goes for elastic events that take place in the thin aluminum target cell.

3. Simulate the HMS more accurately. Currently, the HMS is treated as a simple plane detector. By integrating the magnetic optics of the HMS into the simulation it will be possible to track the particles into the detector hut and introduce the resolution of the detectors. This will also allow future users to track recoil protons back to the target, improving the interaction reconstruction process.

4. Simulate the response of the Calorimeter. Currently, the calorimeter is treated as a simple plane detector. It may be useful to introduce the energy and position resolution of the real the calorimeter to the simulation.

5. Analyze the target magnet shadow. Currently, at kinematics point P2, the target magnet shadows part of the calorimeter as seen from the target cell. The effects of this should be examined in greater detail.

6. Estimate Trigger rates in the calorimeter. Such as estimate has not yet been made using this simulation.

Bibliography

[1] Brodsky, S. J. and G. R. Farrar. *Scaling laws at large transverse momentum.* Phys. Rev. Lett., **31** 1153–1156 (1973).

[2] Brooks, T. C. and L. J. Dixon. *Recalculation of proton compton scattering in perturbative QCD.* Phys. Rev., **D62** 114021 (2000).

[3] Jones, M. K. *et al.*. G_{E_p}/G_{M_p} *ratio by polarization transfer in* $\vec{e}p \to e\vec{p}$. Phys. Rev. Lett., **84** 1398–1402 (2000).

[4] Gayou, O. *et al.*. *Measurement of* G_{E_p}/G_{M_p} *in* $\vec{e}p \to e\vec{p}$ *to* $Q^2 = 5.6\ GeV^2$. Phys. Rev. Lett., **88** 092301 (2002).

[5] Hamilton, D. J., V. H. Mamyan, and the JLab Hall A Collaboration. *Polarization transfer in proton compton scattering at high momentum transfer.* Physical Review Letters, **94** 242001 (2005).

[6] Radyushkin, A. V. *Nonforward parton densities and soft mechanism for form factors and wide-angle compton scattering in QCD.* Phys. Rev., **D58** 114008 (1998).

[7] Huang, H. W., P. Kroll, and T. Morii. *Perturbative and non-perturbative QCD corrections to wide-angle compton scattering.* Eur. Phys. J., **C23** (2002).

[8] Diehl, M., T. Feldmann, R. Jakob, and P. Kroll. *Generalized parton distributions from nucleon form factor data*. Eur. Phys. J., **C39** 1 (2005).

[9] Day, D., B. Wojtsekhowski, *et al.*. *Initial state helicity correlation in wide angle compton scattering* (2005). Submitted to Jefferson Lab PAC28.

[10] Hamilton, D. J. *Polarisation Transfer in Proton Compton Scattering at High Momentum Transfer*. Ph.D. thesis, University of Glasgow (2004).

[11] Brodsky, S. J. and G. P. Lepage. *Helicity selection rules and tests of gluon spin in exclusive QCD processes*. Phys. Rev., **D24** 2848 (1981).

[12] Brodsky, S. J. and G. R. Farrar. *Scaling laws for large momentum transfer processes*. Phys. Rev., **D11** 1309 (1975).

[13] Lepage, G. P. and S. J. Brodsky. *Exclusive processes in perturbative quantum chromodynamics*. Phys. Rev., **D22** 2157 (1980).

[14] Farrar, G. R. and H. Zhang. *Large momentum transfer compton scattering*. Phys. Rev. Lett., **65** 1721–1724 (1990).

[15] Vanderhaeghen, M., P. A. M. Guichon, and J. Van de Wiele. *Compton scattering and the nucleon valence wavefunction*. Nucl. Phys., **A622** 144c–156c (1997).

[16] Diehl, M., T. Feldmann, R. Jakob, and P. Kroll. *Linking parton distributions to form factors and compton scattering*. Eur. Phys. J., **C8** 409–434 (1999).

[17] Radyushkin, A. V. *Scaling limit of deeply virtual compton scattering*. Phys. Lett., **B380** 417–425 (1996).

[18] Radyushkin, A. V. *Nonforward parton distributions*. Phys. Rev., **D56** 5524–5557 (1997).

[19] Ji, X. *Deeply virtual compton scattering.* Phys. Rev., **D55** 7114–7125 (1997).

[20] Ji, X. *Gauge-invariant decomposition of nucleon spin.* Phys. Rev. Lett., **78** 610–613 (1997).

[21] Miller, G. A. *Handling the handbag diagram in compton scattering on the proton.* Phys. Rev., **C69** 052201 (2004).

[22] Shupe, M. A. *et al.. Neutral-pion photoproduction and proton compton scattering at large angles.* Phys. Rev., **D19** 1921–1930 (1979).

[23] Nathan, A., B. Wojtsekhowski, *et al.. Polarization transfer in wide angle compton scattering* (2003). Submitted to Jefferson Lab PAC26.

[24] Crabb, D. G. and D. B. Day. *The Virginia/Basel/SLAC polarized target: Operation and performance during experiment E143 at SLAC.* Nucl. Instrum. Meth., **A356** 9–19 (1995).

[25] Averett, T. D. *et al.. A solid polarized target for high-luminosity experiments.* Nucl. Instrum. Meth., **A427** 440–454 (1999).

[26] Crabb, D. G. and W. Meyer. *Solid polarized targets for nuclear and particle physics experiments.* Ann. Rev. Nucl. Part. Sci., **47** 67–109 (1997).

[27] Perdrisat, C. *et al.. Jefferson Lab experiment E01-109* (2001).

[28] Day, D. (August 2006). Private communication.

[29] Geant4 Collaboration. Geant4 Toolkit (2006).
URL `http://geant4.web.cern.ch/geant4/`

[30] Hubbell, J., H. Gimm, and I. Overbo. *Pair, triplet and total atomic cross sections (and mass attenuation coefficients) for 1 MeV- 100 GeV photons in elements Z=1 to 100*. J. Phys. Chem. Ref. Data, **9** 1023–1147 (1980).

[31] Storm, E. and H. I. Israel. *Photon cross sections from 1 keV to 100 MeV for elements Z=1 to Z=94*. Nucl. Data Tables, **A7** 565–681 (1970).

[32] Geant4 Collaboration. Physics Reference Manual (2006).
URL `http://geant4.web.cern.ch/geant4/support/userdocuments`

[33] Klein, O. and Y. Nishina. Z. Phys., **52** 853–68 (1929).

[34] Heitler, W. *The Quantum Theory of Radiation*. Oxford University Press (1957).

[35] Burkhardt, H., S. R. Kelner, and R. P. Kokoulin. *Monte carlo generator for muon pair production*. CERN-SL-2002-016-AP (2002).

[36] Gavrila, M. *Relativistic k-shell photoeffect*. Phys. Rev., **113** 514–526 (1959).

[37] Messel, H. and D. F. Crawford. *Electron-Photon Shower Distribution Function*. Pergamon Press, Oxford (1970).

[38] Lewis, H. W. *Multiple scattering in an infinite medium*. Phys. Rev., **78** 526–529 (1950).

[39] Yan, C. *et al.*. *Preliminary user's manual for the High Momentum Spectrometer at CEBAF*. Technical report, Continuous Electron Beam Accelerator Facility (Jefferson Lab) (1991).

[40] Oxford Instruments. Target magnet field map, Don Crabb, private communication.

[41] Bodek, A. and J. L. Ritchie. *Further studies of fermi motion effects in lepton scattering from nuclear targets.* Phys. Rev., **D24** 1400 (1981).

[42] ROOT: An Object Oriented Data Analysis Framework (2006).
URL `http://root.cern.ch/`

[43] Ezhela, V. V. and B. V. Polishchuk. *Reanalysis of $e^{\pm}p$ elastic scattering data in terms of proton electromagnetic form factors,* (1999). Hep-ph/9912401.

[44] Brash, E. J., A. Kozlov, S. Li, and G. M. Huber. *New empirical fits to the proton electromagnetic form factors.* Phys. Rev., **C65** 051001 (2002).

[45] Day, D. and B. Wojtsekhowski. *Response to TAC comments for P-05-101* (2005). Private communication.

[46] Danagoulian, A. *Measurements of Compton Scattering on the Proton at 2-6 GeV.* Ph.D. thesis, University of Illinois at Urbana-Champaign (2006).

Appendix A

Simulation Instructions

The computer code used for this simulation can be found as a tarball at

`http://spin.phys.virginia.edu/jlw9p.`

The work directory, realcs/, should contain the following files

`realcs.cc, GNUmakefile, trg_field_map.dat, vis.mac`

and two directories named /src and /include. All of the header files are located in /include and all of the source files are located in /src. To properly compile this program the user's environment must be set up properly. On the JLab linux machines the user must type the command "use geant4/X.X.X" where the X.X.X is the desired version number (v4.6.2 was used by the author). Once the environment variables are set, the command "gmake" should compile the code according to the GNUmakefile and the make files that it calls. This will create a new directory ../Geant4 with two subdirectories /bin and /tmp. /bin contains the realcs executable file and /bin contains all of the object and dependency files from the pieces of source code.

Operation of the simulation is fairly straightforward once a basic understanding of the Geant4 toolkit has been obtained. The detector geometry is defined in realcsDe-

tectorConstruction.cc. The main function is Construct() which initializes the target field and calls the function ConstructAll(). It is called at the start of the program. ConstructAll() then builds the world, the detectors, and the radiator. It also calls the functions that build the rest of the environment. Therefore it is easy to turn off certain pieces of the environment, such as the beam pipes, by simply commenting out the correct function call. realcsPhysicsList is used to define all of the particles and processes desired for the simulation. It also allows the user the set a cuts limit for how far a particle must travel in order to not be killed. This is set with the SetCuts() function.

The heart of the simulation, though is in the realcsPrimaryGeneratorAction. It is here that the type of primary particles is set. This is controlled with the variable primFlag. The options are electronGun, elasticep, elasticgp and piProd. Setting primFlag = electronGun will simulate the electron beam in Hall C. primFlag = elasticep will randomize elastic electron-proton scattering events over the entire target cell. The remaining two options will do the same, but with different scattered particles. All three of these options result in calls the same functions, SetScatteringKin(), which does all of the necessary kinematical calculations. Unfortunately, the initial momentum direction of one of the particles has been hard coded into the program. It is set to match the location of the detectors (defined in realcsDetectorConstruction.cc)

All of this is controlled by the realcs.cc main program. It initializes each necessary structure and sets up the visualization and GUI session. The visualization can be turned off by un-defining G4_VIS_USE at the top of the page. The program can also be set to run in batch mode (without a session) by setting the variable argc to skip the session definition section of code. If the data is to be output to a text file, the file must be opened and closed in realcs.cc in order to clear it. The additional definition of ctSetup() at the bottom of realcs.cc is not strictly necessary. It is only needed to

ensure that the code will compile properly on JLab computers.

The most common output used during the development of this simulation was a file output system set in realcsSteppingAction.cc. Basically, all the information about the step is available here and is appended to the existing data file if the requirements are met. This is the place to apply some initial thresholds and data cuts. The less information that is printed to the file, the faster the program will run. Another tip for increasing the speed is to turn off the event drawing functionality in realcsEventAction.cc. If the visualization is turned on this will keep the program from drawing every single particle track and cut the computation time by over 50%.

If it is desirable to run in batch mode, the commands must be inserted into the appropriate portion of realcs.cc. The program will execute these commands in order then delete all of its structures and close itself. If, instead, running a full Geant4 session is desirable, only the

```
``session->StartSession();''
```

line need be in place. This will give the use a command prompt and access to all of the in-situ controls. Typing "help" will display a list of help topics which will lead the user to every viable command that can be run in the session. The user may even define his own commands via the various Messenger pieces of source code. The most important command is run/beamOn *, where the * represents the number of primary events to generate.

Compiling a program of this complexity can prove to be difficult. It is suggested that the novice user first attempt to compile and run one of the novice examples on a computer that is known to have a proper library setup. Because of the immense number of files involved most users choose to compile using shared libraries. These libraries include the object and dependency files for every piece of source code in the

Geant4 installation. By using these shared libraries, the user only needs to compile the pieces of code that the user actually writes. The GNUmakefile that is included is designed for efficiency as well. It ensures that each time the program is compiled only those files that have changed will be re-compiled. This can occasionally cause a problem where changed files are not re-compiled as they should be. If this problem should occur, the user must delete all of the user object files. Another important issue is that every time the Geant4 program is started it begins with the same random number seeds, unless told to do otherwise. It is possible to have the program print out the random number seeds used on the last event in a previous run. If these seeds are then used via the session command

```
random/resetEngineFrom *.rndm
```

Geant4 will essentially pick up where it left off and not repeat any events (*.rndm is the name of the file where the seeds are stored.) In this way it is also possible to save entire simulation runs for replay at a later time.